The Astrophysical Journal, 888:55 (19pp), 2020 January 10 https://doi.org/10.3847/1538-4357/ab5dc4


# The *Gaia*–ESO Survey: Carbon Abundance in the Galactic Thin and Thick Disks*

Mariagrazia Franchini[1], Carlo Morossi[1], Paolo Di Marcantonio[1], Miguel Chavez[2], Vardan Zh. Adibekyan[3], Amelia Bayo[4,5], Thomas Bensby[6], Angela Bragaglia[7], Francesco Calura[7], Sonia Duffau[8], Anais Gonneau[9], Ulrike Heiter[10], Georges Kordopatis[11], Donatella Romano[7], Luca Sbordone[12], Rodolfo Smiljanic[13], Gražina Tautvaišienė[14], Mathieu Van der Swaelmen[15], Elisa Delgado Mena[3], Gerry Gilmore[16], Sofia Randich[17], Giovanni Carraro[18], Anna Hourihane[16], Laura Magrini[15], Lorenzo Morbidelli[15], Sérgio Sousa[19], and C. Clare Worley[16]

[1] INAF—Osservatorio Astronomico di Trieste, Via G.B. Tiepolo 11, Trieste, I–34143, Italy; Mariagrazia.franchini@inaf.it
[2] Instituto Nacional de Astrofísica, Óptica y Electrónica, Luis Enrique Erro 1, 72840 Tonantzintla, Puebla, Mexico
[3] Centro de Astrofísica da Universidade do Porto, Rua das Estrelas, 4150-762 Porto, Portugal
[4] Instituto de Física y Astronomía, Universidad de Valparaíso, Avda. Gran Bretaña 1111, Valparaíso, Chile
[5] Núcleo Milenio de Formación Planetaria, NPF, Universidad de Valparaíso, Chile
[6] Lund Observatory, Department of Astronomy and Theoretical Physics, Box 43, SE-221 00 Lund, Sweden
[7] INAF—Osservatorio di Astrofisica e Scienza dello Spazio di Bologna, Via Gobetti 93/3 I-40129 Bologna, Italy
[8] Universidad Andrés Bello Departamento de Ciencias Fernandez Concha 700, Las Condes Santiago, Chile
[9] Institute of Astronomy, University of Cambridge, Madingley Road, Cambridge CB3 0HA, UK
[10] Observational Astrophysics, Department of Physics and Astronomy, Uppsala University, Box 516, 75120 Uppsala, Sweden
[11] Université Côte d'Azur, Observatoire de la Côte d'Azur, Laboratoire Lagrange, CNRS UMR 7293 CS 34229 06304 Nice Cedex 04, France
[12] European Southern Observatory, Alonso de Cordova 3107 Vitacura, Santiago de Chile, Chile
[13] Nicolaus Copernicus Astronomical Center, Polish Academy of Sciences, ul. Bartycka 18, 00-716, Warsaw, Poland
[14] Institute of Theoretical Physics and Astronomy, Vilnius University, Sauletekio av. 3, 10258, Vilnius, Lithuania
[15] INAF—Osservatorio Astrofisico di Arcetri, Largo E. Fermi 5, Florence I-50125, Italy
[16] Institute of Astronomy, University of Cambridge, Madingley Road, Cambridge CB3 0HA, UK
[17] INAF—Osservatorio Astrofisico di Arcetri, Largo E. Fermi 5, I-50125, Florence, Italy
[18] Dipartimento di Fisica e Astronomia, Università di Padova, Vicolo dell'Osservatorio 3, Padova, I-35122, Italy
[19] Instituto de Astrofísica e Ciências do Espaço, Universidade do Porto, CAUP, Rua das Estrelas, 4150-762 Porto, Portugal
*Received 2019 October 29; revised 2019 November 26; accepted 2019 November 29; published 2020 January 8*

## Abstract

This paper focuses on carbon, which is one of the most abundant elements in the universe and is of high importance in the field of nucleosynthesis and galactic and stellar evolution. The origin of carbon and the relative importance of massive and low- to intermediate-mass stars in producing it is still a matter of debate. We aim at better understanding the origin of carbon by studying the trends of [C/H], [C/Fe], and [C/Mg] versus [Fe/H] and [Mg/H] for 2133 FGK dwarf stars from the fifth *Gaia*–ESO Survey internal data release (GES iDR5). The availability of accurate parallaxes and proper motions from *Gaia* DR2 and radial velocities from GES iDR5 allows us to compute Galactic velocities, orbits, absolute magnitudes, and, for 1751 stars, Bayesian-derived ages. Three different selection methodologies have been adopted to discriminate between thin- and thick-disk stars. In all the cases, the two stellar groups show different [C/H], [C/Fe], and [C/Mg] and span different age intervals, with the thick-disk stars being, on average, older than the thin-disk ones. The behaviors of [C/H], [C/Fe], and [C/Mg] versus [Fe/H], [Mg/H], and age all suggest that C is primarily produced in massive stars. The increase of [C/Mg] for young thin-disk stars indicates a contribution from low-mass stars or the increased C production from massive stars at high metallicities due to the enhanced mass loss. The analysis of the orbital parameters $R_{\rm med}$ and $|Z_{\rm max}|$ supports an "inside–out" and "upside–down" formation scenario for the disks of the Milky Way.

*Unified Astronomy Thesaurus concepts:* Late-type stars (909); Stellar abundances (1577); Stellar ages (1581); Galaxy stellar content (621)

## 1. Introduction

The present chemical composition of stars in the Milky Way (with the exception of hydrogen, helium, and trace amounts of lithium and beryllium produced during the formation of the universe) comprises various nucleosynthetic products forged in previous generations of stars. Since the production history of each element can follow different nucleosynthesis pathways (probing different astrophysical processes, sites, timescales, and/or stellar-progenitor masses), all of the elements play potentially important roles in our understanding of Galactic chemical evolution (GCE). However, in this work we focus on carbon, which, next to hydrogen, helium (actually linked to the big bang), and oxygen, is the most abundant element in the universe and is of high importance in the field of galactic nucleosynthesis, stellar evolution, exoplanets, and astrobiology.

Even nowadays, the origin of carbon is somewhat uncertain, and the relative importance of massive and low- to intermediate-mass stars is still a matter of debate. Gustafsson et al. (1999) conclude that carbon is mainly contributed from superwinds of metal-rich massive stars, and not from low-mass stars. Chiappini et al. (2003b), Matteucci & Chiappini (2003), Chiappini et al. (2003a), Bensby & Feltzing (2006), and Mattsson (2010) find strong indications that carbon is produced in low- and intermediate-mass stars. Shi et al. (2002) find that carbon is contributed by superwinds of metal-rich massive ($M > 8\,M_{\odot}$) stars in the early stages of disk formation in the Galaxy, while a significant amount of carbon is

* Based on observations collected with the FLAMES instrument at VLT/UT2 (Paranal Observatory, ESO, Chile), for the *Gaia*–ESO Large Public Spectroscopic Survey (188.B-3002, 193.B-0936).

contributed by low-mass stars in later stages. Other works in the literature favor different mixtures between the relative importance of massive and low- to intermediate-mass stars (e.g., Liang et al. 2001; Akerman et al. 2004; Gavilán et al. 2005), while others (e.g., Henry et al. 2000; Carigi et al. 2005) suggest massive stars as the main carbon source. In any case, it is important to notice that the relative contributions from low- to intermediate-mass stars and massive stars depend strongly on the age and past evolutionary rate of the stellar system that is being scrutinized; hence, the conclusions drawn for the solar vicinity do not necessarily hold for any other system and/or Galactic region (Carigi et al. 2005; Romano et al. 2019).

Different views on the relative role of high-mass and intermediate- to low-mass stars have reflected uncertainties on the carbon production, the dredge-up and rotation effects, stellar yields, and metallicity-dependent mass loss from stars of different mass and chemical composition (e.g., Meynet & Maeder 2002; van den Hoek & Groenewegen 1997). Additionally, significant uncertainties on the observed carbon abundances have hindered the checks of compatibility between theoretical results and those obtained empirically. Nucleosynthesis and Galactic evolution of C can be studied by determining its abundance mainly in main-sequence stars (with different ages and metallicities) of spectral types F, G, and K because their atmospheres still present essentially the original chemical composition of their birth sites. However, there is still considerable uncertainty about the abundances of C because of inaccuracy of oscillator strengths ($\log gf$), incompleteness of the available atomic and molecular lines, dependence of results from non-LTE (NLTE) corrections, and atmospheric models applied (Asplund 2005; Amarsi et al. 2019b, 2019c). The spectral lines invoked to spectroscopically determine the abundance of carbon, such as atomic lines (C I) or molecular lines (CH, $C_2$, CO), have different characteristics, depending on the type of stars, in terms of the sensitivity to 3D and/or NLTE effects.

So far, carbon abundance determination from high-resolution spectra of F and G main-sequence stars in the solar neighborhood has not provided consistent results. Reddy et al. (2006) and Nissen et al. (2014) have found evidence of a systematic difference in the trend of [C/Fe] versus [Fe/H] between thin- and thick-disk stars. The work of Reddy et al. (2006) is based on a sample of about 200 thin-disk stars and 100 thick-disk stars, whose membership to the thin- or thick-disk sample is based on their kinematics, while Nissen et al. (2014) use two smaller samples of stars (57 and 25 thin- and thick-disk stars, respectively) selected using the [$\alpha$/Fe]–[Fe/H] diagram as described by Adibekyan et al. (2013). In disagreement with the results of these studies, Bensby & Feltzing (2006) show almost flat and totally merged trends of [C/Fe] below [Fe/H] $\approx -0.2$ dex for thin- and thick-disk stars. Their work is based on the analysis of the [C I] line at 8727 Å, which is almost not affected by NLTE effects (see Amarsi et al. 2019a), for a small sample of 35 thin-disk stars and 16 thick-disk stars selected by using their kinematics and observed with high signal-to-noise ratio (S/N $> 300$) and high resolution ($R \sim 220{,}000$).

Since the trend of [C/H] with time or metal abundance [Fe/H] is currently not well constrained by stellar and galactic evolution models, much more insight should be gained from observations. With the advent of large spectroscopic surveys, such as *Gaia*–ESO (GES; Gilmore et al. 2012; Randich et al. 2013, ESO programs 188.B-3002 and 193.B-0936), APOGEE (Majewski et al. 2017), and GALAH (De Silva et al. 2015), it is now possible to investigate, by using sizable statistical samples, the behavior of carbon in different populations of our Galaxy. Among several ongoing spectroscopic surveys, GES has provided high-resolution spectra of stars belonging to various stellar populations of our Galaxy using the spectrograph FLAMES@VLT (Pasquini et al. 2002). GES aims at homogeneously deriving stellar parameters and abundances in a large variety of environments, including the major Galactic components (thin and thick disks, halo, and bulge), open and globular clusters, and calibration samples. The higher-resolution spectra obtained with UVES (Dekker et al. 2000) allow the determination of the abundances for more than 30 different elements, including carbon.

In this paper we derive additional information on carbon abundances based on the trends of [C/H], [C/Fe], and [C/Mg] versus [Fe/H], [Mg/H], and age for stars in the Galactic disks by using a large sample of 2133 FGK dwarf stars whose spectra were extracted from the fifth *Gaia*–ESO Survey internal data release (GES iDR5). We decided to use only dwarf stars and exclude red giants in which the atmospheric carbon and nitrogen abundances are affected by internal mixing of material during the first dredge-up phase (Iben 1965). This material from the core has been enriched through the CN cycle, which results in a buildup of N and a depletion of C. The depth of the convective zone during the first dredge-up phase is dependent on the mass of the star, resulting in decreasing atmospheric C-to-N ratios in red giants (see Salaris et al. 2015, for a detailed explanation).

Most of the stars in our sample have accurate parallaxes and proper motions available from the second *Gaia* data release (DR2; Gaia Collaboration et al. 2018). The *Gaia* DR2 database provides a high-precision parallax and proper-motion catalog for over 1 billion sources, supplemented by precise and homogeneous multiband all-sky photometry and a large radial velocity survey at the bright ($G \lesssim 13$) end. The availability of precise fundamental astrophysical information required to map and understand the Milky Way is thus expanded to a very substantial fraction of the volume of our Galaxy, well beyond the immediate solar neighborhood. The knowledge of accurate parallaxes and proper motions from *Gaia* DR2 and radial velocities from GES iDR5 allows us to compute Galactic velocities, orbits, and absolute magnitudes for 1804 stars and then, by using a Bayesian approach, ages for 1751 of them. In Section 2 we present the starting stellar sample as obtained from GES iDR5 and the determination of carbon abundance. In Section 3 we define the samples of thin- and thick-disk stars using three different selection methodologies. In Sections 4 and 5 we discuss the kinematical and chemical properties of the selected samples. Section 6 presents the trends of [C/H], [C/Fe], [C/Mg], $R_{\rm med}$, and $|Z_{\rm max}|$ with stellar ages for the thin- and thick-disk stars, and conclusions are given in Section 7.

## 2. The UVES–U580 Stellar Sample Definition

We used the GES iDR5 internal release to extract the observed spectra of all the FGK dwarf stars obtained with the UVES spectrograph in a setup centered at 580 nm (hereafter UVES–U580 sample) at a resolution $R \sim 47{,}000$. The spectra were exposed onto two CCDs, resulting in a wavelength coverage of 4700–6840 Å with a gap of about 50 Å in the center. Data reduction of the UVES spectra has been performed

using a workflow specifically developed for this project (Sacco et al. 2014). The GES iDR5 release contains, together with the stacked spectra and the tables of metadata summarizing these spectra, also radial ($V_r$) and rotational velocities ($v \sin i$), recommended stellar atmosphere parameters (effective temperature, $T_{\rm eff}$, surface gravity, $\log g$, iron abundance, [Fe/H], and microturbulence, $\xi$), and individual element abundances,[20] including carbon. The UVES–U580 spectra were analyzed with the *Gaia*–ESO multiple pipelines strategy, as described in Smiljanic et al. (2014). The results of each pipeline are combined with an updated methodology to define the final set of recommended values of the atmospheric parameters and chemical abundances that are part of GES iDR5 (see also Magrini et al. 2017, A. Hourihane et al. 2019, in preparation). Average uncertainties in the atmospheric parameters are 55 K, 0.13 dex, and 0.07 dex for $T_{\rm eff}$, $\log g$, and [Fe/H], respectively (Magrini et al. 2018).

### 2.1. Stellar Parameters

A first sample of dwarf stars was obtained by performing a Structured Query Language search to select all the stars in the 3750–7000 K and 3.50–5.00 dex effective temperature and surface gravity ranges[21] observed with the U580 setup and characterized by an S/N greater than 10. Then, we removed all the stars with some peculiarity or binarity flag, with a lack of error estimates of the stellar atmosphere parameter values, or without iron abundances from Fe I or Fe II lines, getting a sample of 2261 stars. In this way we obtained a sample well suitable for our analysis since it contains objects with homogeneously determined $T_{\rm eff}$, $\log g$, [Fe/H], and detailed chemical composition, spanning the following ranges: $T_{\rm eff}$ from 3779 to 6868 K, $\log g$ from 3.50 to 4.80 dex, and [Fe/H] from $-2.44$ to $+0.60$ dex. The atmospheric parameter coverage is shown in Figure 1. In the following, to work with a statistically significant data set, we limit our analysis to stars with $T_{\rm eff} > 4450$ K and [Fe/H] $> -1.0$ dex, thus reducing the sample to a total of 2248 stars.

### 2.2. Carbon Abundances

Out of the 2248 stars in our sample, 1936 have an estimate of carbon abundance from atomic lines in GES iDR5. The abundance determination of C is quite challenging, and the values of C/H derived by GES iDR5 are, in general, less accurate than the corresponding values for the other elements. In particular, the estimated "C1" GES iDR5 carbon abundance for the stars in our sample is based on the analysis of only two (1500 stars) or even one (436 stars) spectral line. The "C1Err" uncertainties are estimated considering the errors on the atmospheric parameters and random errors (mainly caused by uncertainties of the continuum placement and by the S/N) and span a range from 0.01 to 0.58 dex, with the bulk of data at 0.05 dex.

It is worthwhile to point out that most of the C/H values were derived by using synthetic spectra computed from MARCS atmosphere models without full consistency between the chemical composition used to build the atmosphere structure and the one actually used in synthesizing the emergent spectrum. In fact, even if MARCS models use the opacity sampling method, GES Working Groups (WGs) adopted grids of models with fixed chemical composition to derive the stellar abundances without any iterative procedure, i.e., without injecting the derived abundances in the atmosphere models and recomputing the atmosphere structure and abundances until consistency is achieved. Such an inconsistency may introduce systematic errors in the abundance determination, in particular when dealing with elements like carbon that may affect significantly the overall opacity. Therefore, in order to remove such an uncertainty, and with the goal of increasing the number of stars in our sample with determined C/H, we decided to reanalyze all their spectra.

#### 2.2.1. Model Atmosphere and Synthetic Spectra

To estimate C/H abundances, we used the stellar atmosphere ATLAS12 code (Kurucz 2005) and the spectral synthesis program SPECTRUM v2.76f (Gray & Corbally 1994) to compute for each of the 2248 stars, assuming different C/H values, its model atmosphere and theoretical spectrum, respectively.

We used ATLAS12 since it allows us to generate ad hoc atmospheric models for any individual element chemical composition and microturbulence parameter ($\xi$), through the OS technique. As a starting point, we adopted for the reference solar abundances those obtained by Grevesse et al. (2007), which have a wide consensus in the literature and whose validity is also confirmed, within the quoted uncertainties, by the abundance determinations derived by Working Group 11 (WG11) of the *Gaia*–ESO consortium (Magrini et al. 2017) from the analysis of UVES spectra of the Sun and M67 giant stars obtained with the U580 and U520 setups.[22] Then, for each $i$th star, we used its GES iDR5 atmospheric parameter values ($T_{\rm eff}$, $\log g$, [Fe/H], and $\xi$) and individual element abundances except for C (for those elements with no estimate of [X/Fe] we assumed [X/Fe] = 0). For each star the atmosphere model was calculated starting from the closest model, in the atmosphere parameter space, among those used for calculating the INTRIGOSS high-resolution synthetic spectral library (Franchini et al. 2018). Its convergence was checked according to the convergence criteria recommended in the ATLAS cookbook.[23] In general, a model is accepted if, at the end of the computing iteration, the flux and the flux derivative errors are, for each layer, below 1% and 10%, respectively. Only for a few models (among the coldest) did we need to significantly increase the number of iterations from the standard figure of 25 to reach the convergence. Eventually, a further check on the reliability of the new obtained ATLAS12 models was done by looking, for each of them, at the behaviors of temperature, gas pressure, electron density, Rosseland absorption coefficient, and radiation pressure at all Rosseland optical depths.

Then, to obtain the corresponding emergent flux and normalized spectrum, we used SPECTRUM v2.76f. The SPECTRUM code calculates an LTE synthetic spectrum starting from a given model atmosphere. The code also requires a line list of atomic and molecular transitions, and we used the INTRIGOSS line list, whose accuracy was established in Franchini et al. (2018).[24] SPECTRUM was used

[20] All abundances of element X are given in the following format: $\log \epsilon_X = \log \frac{N_X}{N_H} + 12.0$.

[21] Effective temperature and surface gravity ranges approximately covered by F, G, and K dwarf stars.

[22] https://www.eso.org/sci/facilities/paranal/instruments/uves/doc.html

[23] http://atmos.obspm.fr/index.php/documentation

[24] http://archives.ia2.inaf.it/intrigoss/

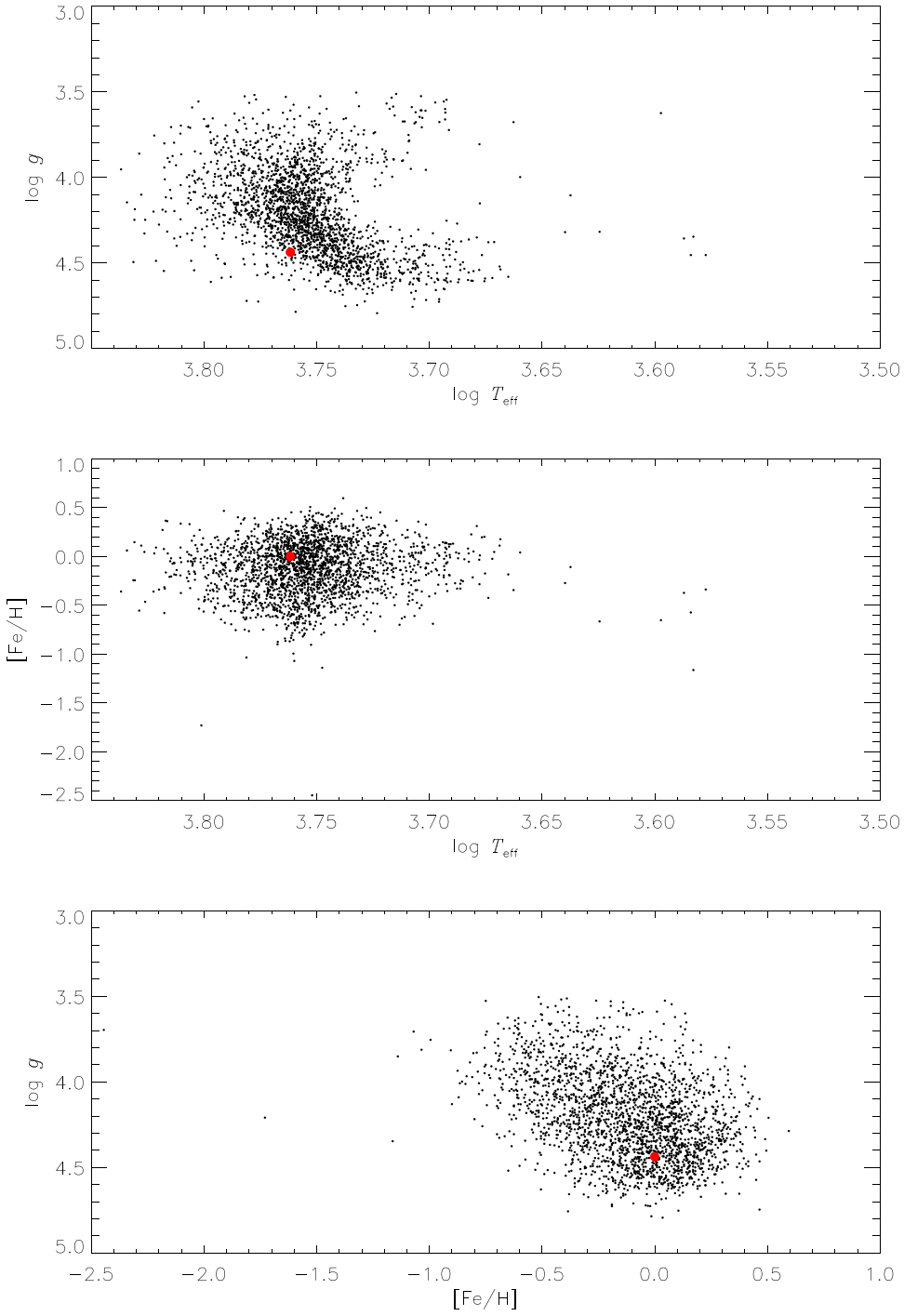


**Figure 1.** GES iDR5 atmospheric parameters of the original sample of 2261 dwarf stars (black points) with the Sun position superimposed (red circle): log $g$ vs. log $T_{\rm eff}$ (top panel); [Fe/H] vs. log $T_{\rm eff}$ (middle panel); log $g$ vs. [Fe/H] (bottom panel).

to deliver both the stellar-disk-integrated normalized spectrum, $S_N$, and the absolute monochromatic flux at the stellar surface, $S_F$, in the spectral range 4830–5400 Å. In particular, we computed for each star a set of 11 models and synthetic spectra with $[C/Fe]_j = -0.5 + (j-1) \times 0.1$ dex (with $j = 1, ..., 11$) and the model and synthetic spectrum, $S_N^{i,GES}$, computed at the GES iDR5 [C/Fe] ratio when available. The use of ATLAS12 and SPECTRUM v2.76f codes, which allowed us to specify the same microturbulence and individual element abundances in deriving both the atmosphere structure and the synthetic spectrum, guarantees the full consistency between atmosphere models and synthetic spectra. Eventually, since the synthetic spectra were computed at a resolving power $R \sim 240{,}000$, they were broadened by using the GES iDR5 $v \sin i$ stellar values and degraded at the resolution of UVES spectra ($R \sim 47{,}000$).

In order to remove the instrumental signature in the observed (stacked) UVES–U580 spectra, we used, for each star $i$, the $j$ normalized synthetic $S_N^{i,j}$ spectra to obtain from the

**Table 1**
Wavelength Regions Used to Estimate [C/Fe] via Comparison of Synthetic and Observed Normalized Spectra

| Wavelength Region (Å) | C I Lines (Å) | log *gf* | References |
|---|---|---|---|
| 4930–4935 | 4930.276 | −3.480 | Kurucz & Peytremann (1975) |
| | 4932.039 | −1.684 | this work |
| | 4934.301 | −4.930 | Kurucz & Peytremann (1975) |
| 5022–5027 | 5023.849 | −2.400 | Kurucz & Bell (1995) |
| | 5024.916 | −2.700 | Kurucz & Bell (1995) |
| 5038–5043 | 5039.057 | −2.200 | this work |
| | 5039.100 | −2.286 | Miller et al. (1974) |
| | 5039.919 | −3.940 | Kurucz & Bell (1995) |
| | 5040.134 | −2.500 | Kurucz & Bell (1995) |
| | 5040.765 | −2.600 | Kurucz & Bell (1995) |
| | 5041.481 | −1.700 | Kurucz & Bell (1995) |
| | 5041.796 | −2.500 | Kurucz & Bell (1995) |
| 5050–5055 | 5051.579 | −2.480 | Kurucz & Peytremann (1975) |
| | 5052.142 | −1.303 | this work |
| | 5053.515 | −1.555 | this work |
| | 5054.619 | −3.690 | Kurucz & Peytremann (1975) |
| 5378–5383 | 5378.921 | −4.640 | Kurucz & Peytremann (1975) |
| | 5380.224 | −2.030 | Kurucz & Peytremann (1975) |
| | 5380.265 | −2.820 | Kurucz & Peytremann (1975) |
| | 5380.312 | −1.692 | this work |

corresponding observed UVES–U580 one a set of normalized observed spectra ($O_N^{i,j}$). The normalization was performed by applying the technique described in Franchini et al. (2018). We searched for quasi-continuum flux reference points in $S_N^{i,j}$ (i.e., wavelength points with flux levels in excess of 0.95), and we used the same points in the corresponding observed UVES spectrum to derive the continuum shape via a low-order polynomial fitting of the ratio between observed and synthetic spectra. Eventually, the observed spectrum is divided by the so-computed polynomial to obtain the normalized spectrum $O_N^{i,j}$. With this technique of matching the continuum levels of observed and corresponding synthetic spectra, we also obtained the observed "flux-calibrated" spectra $O_F^{i,j}$ by using the ratio between the observed UVES spectrum and the corresponding $S_F^{i,j}$ in the same reference points previously defined via $S_N^{i,j}$.

### 2.2.2. [C/Fe] Determination

For carbon abundance determination we used a spectrum synthesis technique. We identify five wavelength regions listed in Table 1, characterized by higher sensitivity to C abundance because of the presence of relatively strong C I lines. We look at each *i* star, and for each *j* pair of spectra, i.e., for different [C/Fe] values, we computed the total standard deviation ($\sigma_j^i$) between $O_N^{i,j}$ and $S_N^{i,j}$ in these wavelength regions. Then, using a parabolic fitting, we determine the "best" [C/Fe] value corresponding to the position of the minimum (if any) of $\sigma_j^i$ versus [C/Fe].

First of all, we fine-tuned the log *gf* of the C I lines by using the same technique described in Franchini et al. (2018), i.e., by comparing the synthetic solar spectrum with an observed one with S/N ∼ 4000 after degrading both of them at the UVES–U580 resolution. The so-obtained (and used in our analysis) log *gf* (15 lines did not need any log *gf* tuning) are reported in Table 1, and we point out that our astrophysical log *gf* values for the only two of our lines that are flagged "recommended (*Y*)" in the GES database are in good agreement with those reported in the Table "LineList" of GES iDR5. Then, the above-described procedure was applied to the solar spectra and led to [C/Fe] = 0.01 dex for the Sun, thus assessing the absence of a systematic offset in the derived [C/Fe] values.

Eventually, we were able to obtain for 2133 stars fiducial [C/Fe] values whose uncertainties we fixed, to be conservative, at ±0.05 dex, i.e., a half-step in our [C/Fe] grid of models and synthetic spectra. No clear minimum in $\sigma_j^i$ was detected for the other 115 stars, thus preventing a sound determination of [C/Fe]. Some examples of the adopted procedure are shown in Figure 2.

In order to double-check the derived carbon abundances, we computed, on the basis of these updated [C/Fe] values, new (hereafter "best") model atmospheres and synthetic spectra, $S_N^{i,best}$ and $S_F^{i,best}$, for each of the 2133 stars and compared them with the observed spectra in the five wavelength regions sensitive to C abundance. The validity of the [C/Fe] values was confirmed by the good agreement between observed and synthetic spectra (see Figure 2). We also computed the $\sigma_{best}^i$ values and $\sigma_{GES}^i$ values for the 1870 stars that have both our and the GES iDR5 estimate of C/H. Figure 3 shows that $S_N^{i,best}$ spectra reproduce as well as the $S_N^{i,GES}$ the observed spectra for 1143 stars ($\sigma_{GES}^i - \sigma_{best}^i < 0.002$). For the other 727 stars $\sigma_{best}^i$ is smaller than $\sigma_{GES}^i$, indicating that our estimates of C/H are more accurate than those reported in the GES iDR5 "RecommendedAstroAnalysis" table.

Since the UVES–U580 spectra contain the $C_2$ bands of the Swan system (Swan 1857) and, in particular, the one used by Gonneau et al. (2016, Table 2) to define the C2U index (bandpass feature: 5087–5167 Å; bandpass "continuum": 5187–5267 Å), we decided to use the C2U index to further check our [C/Fe] determinations. In this way we will use $C_2$ molecular features to verify our C abundances, which are based on atomic lines. We computed for the 2133 stars the C2U index from both $S_F^{i,best}$ and $O_F^{i,best}$ obtained as described in Section 2.2.1. Figure 4 shows the distribution of the differences between the synthetic and the observational C2U index values. As can be seen, in most cases the differences are within $3\sigma_{\Delta C2U} = 0.036$ mag (there are only 66 stars, 3% of the total, that show larger differences). By comparing this figure with Figure 5 in Franchini et al. (2018), it can be noticed that the outliers with $\Delta_{C2U}$ larger, in absolute value, than 0.1 mag have disappeared and that the bulk of the data are now within ±0.036 instead of ±0.05. The largest differences are for the stars with [Fe/H] $\gtrsim$ +0.2 dex. We recall that the strength of $C_2$ lines depends not only on carbon abundance but also, indirectly, on nitrogen and oxygen abundances because of the competing role of CN and CO. In Figure 5 we show the effect, on $C_2$ and C I lines, of different oxygen abundances in the $S_N^{best}$ of the star 09473303-1018485 (also shown in Figure 2). Three synthetic spectra were computed by using [O/Fe] = −0.4, 0.0, and +0.4 with the same [C/Fe] = −0.21. As can be seen, the strength of the $C_2$ lines (top panel) is different for the different [O/Fe] values, i.e., as expected, lower [O/Fe] lead to stronger $C_2$ lines. On the other hand, the atomic C I lines (bottom panel) are unaffected by the oxygen abundance (the three different synthetic spectra plotted with different colors practically coincide). Actually, the sensitivity of the $C_2$ lines to the

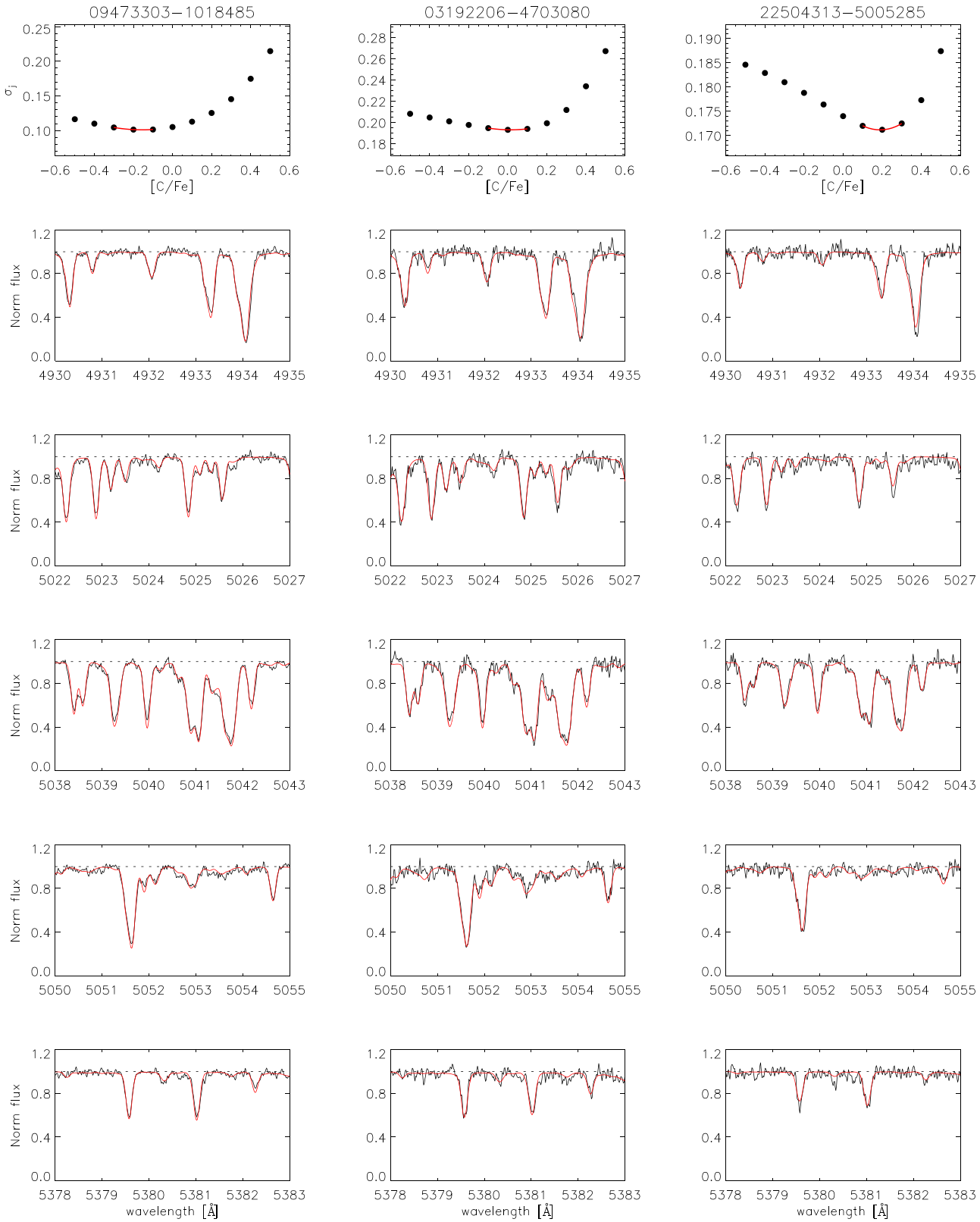


**Figure 2.** Examples of determination of [C/Fe] for three stars. Top panels: trends of $\sigma_j$ vs. [C/Fe] (black dots) and parabolic interpolations (red lines); other panels: comparison between observed spectra (black lines) and corresponding synthetic ones (red lines) computed with the "best" [C/Fe] (see text).

oxygen abundance is the reason why we preferred to derive carbon abundances from atomic lines instead of using molecular ones even if atomic lines may be affected by NLTE (see discussion below).

The small differences shown in Figure 4 indicate that, in any case, our estimates of [C/Fe] reproduce in an acceptable way not only the C I atomic lines but also the strength of the $C_2$ Swan bands. This fact suggests that in our "best" models and

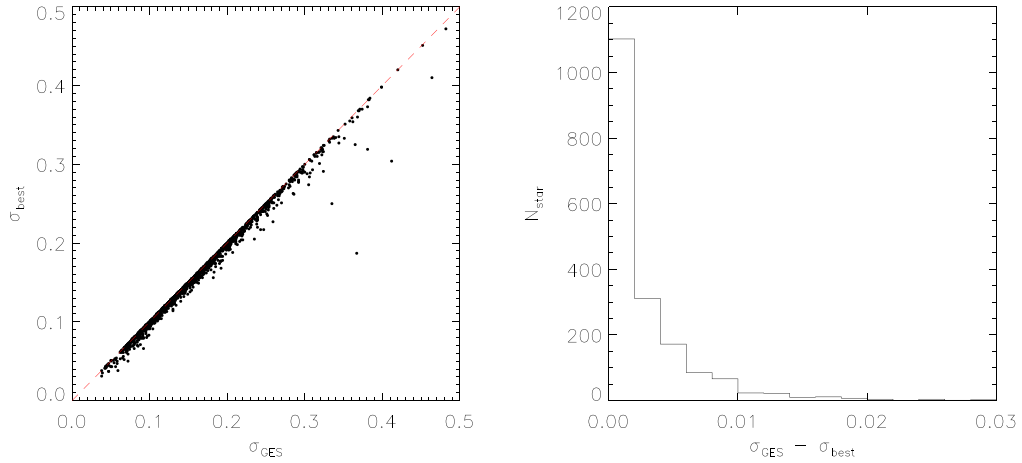


**Figure 3.** Comparison between $\sigma^i_{\rm best}$ and $\sigma^i_{\rm GES}$ for the 1870 stars with [C/Fe] from this paper and from GES iDR5 (left panel) and distribution of the differences $\sigma^i_{\rm GES} - \sigma^i_{\rm best}$. Eleven stars with differences greater than 0.03 were excluded from the distribution plot to increase readability.

**Table 2**
Dispersion Velocities

| | $\sigma_U$ km s$^{-1}$ | $\sigma_V$ km s$^{-1}$ | $\sigma_W$ km s$^{-1}$ | $N_{\rm star}$ |
|---|---|---|---|---|
| Thin$^{\rm C}$ | 42 | 27 | 21 | 1065 |
| Thin$^{\rm K}$ | 38 | 23 | 17 | 1356 |
| Thin$^{\rm O}$ | 31 | 20 | 18 | 934 |
| Thin$^{\rm S}$ | 39 | 20 | 20 | |
| Thin$^{\rm B}$ | 35 | 20 | 16 | |
| Thick$^{\rm C}$ | 64 | 48 | 41 | 92 |
| Thick$^{\rm K}$ | 68 | 42 | 51 | 196 |
| Thick$^{\rm O}$ | 86 | 45 | 41 | 90 |
| Thick$^{\rm S}$ | 63 | 39 | 39 | |
| Thick$^{\rm B}$ | 67 | 38 | 35 | |

**Note.** Thin$^{\rm S}$ and Thick$^{\rm S}$ from Soubiran et al. (2003); Thin$^{\rm B}$ and Thick$^{\rm B}$ from Bensby et al. (2014).

synthetic spectra we used acceptable estimates of N/H and O/H even if no detailed information on nitrogen and oxygen abundance is available in GES for our stars.

Recent studies in late-type stars have demonstrated the potentially large impact of 3D-NLTE effects on carbon abundance determination (e.g., Amarsi et al. 2019a). The paper by Amarsi et al. (2019c) shows that in the metallicity regime of our stars ([Fe/H] $> -1$) the 3D-NLTE corrections do not change significantly the [C/Fe] ratios (see their Figure 11). Their paper provides, in any case, a tool to correct 1D-LTE carbon abundances to take into account the 3D-NLTE effects. We used a code kindly provided to us by A. M. Amarsi (2019, private communication) to compute for all our stars the required 3D-NLTE corrections. It is worth noticing that our C/H estimates were not derived from equivalent width measurements and that Amarsi et al. (2019c) provide corrections only for two C I lines given in Table 1, thus compelling us to consider the corrections only as a first approximation. The corrections we computed are all between $\pm 0.05$ dex, i.e., of the order of our uncertainties. Moreover, we did not find any systematic difference in the corrections between the thin- and thick-disk samples defined in Section 3 (for the actual values see Sections 3.1–3.3). In the following we will use our atomic 1D-LTE C/H values for comparing overall trends since

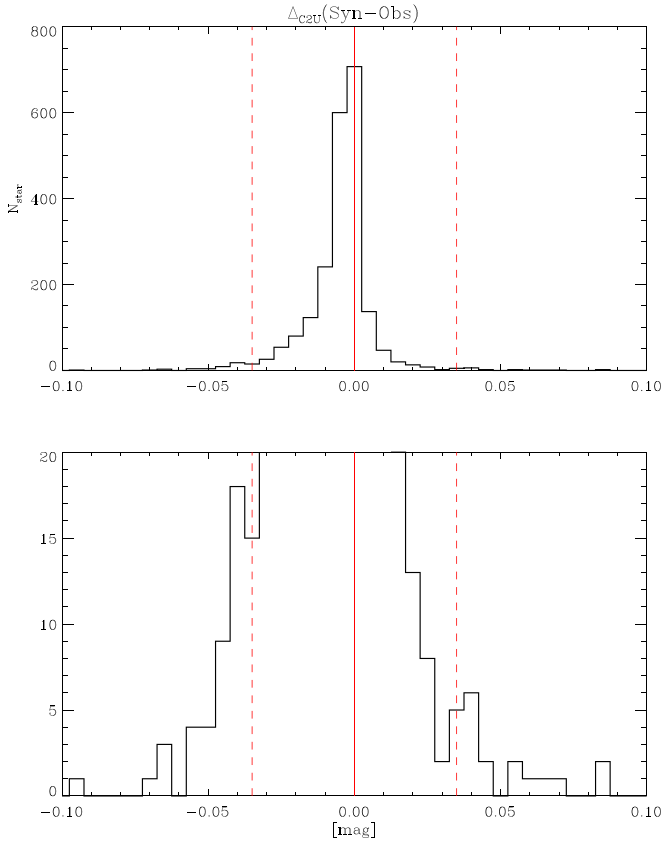


**Figure 4.** Distribution of the differences between C2U indices derived for each pair of "best" [C/Fe] synthetic and UVES–U580 spectra; the bottom panel zooms in on the $y$-scale and shows the presence of a few stars with $\Delta_{\rm C2U}$ values outside $3\sigma_{\Delta \rm C2U}$ (red dashed lines).

3D-NLTE corrections do not significantly affect, at least in a first approximation, our results.

## 3. Thin- and Thick-disk Samples

In this paper we want to investigate whether there is any difference in the C abundance behavior in stars belonging to the thin or to the thick Galactic disk. To achieve this goal, we need to select the stars in our sample that are part of each disk

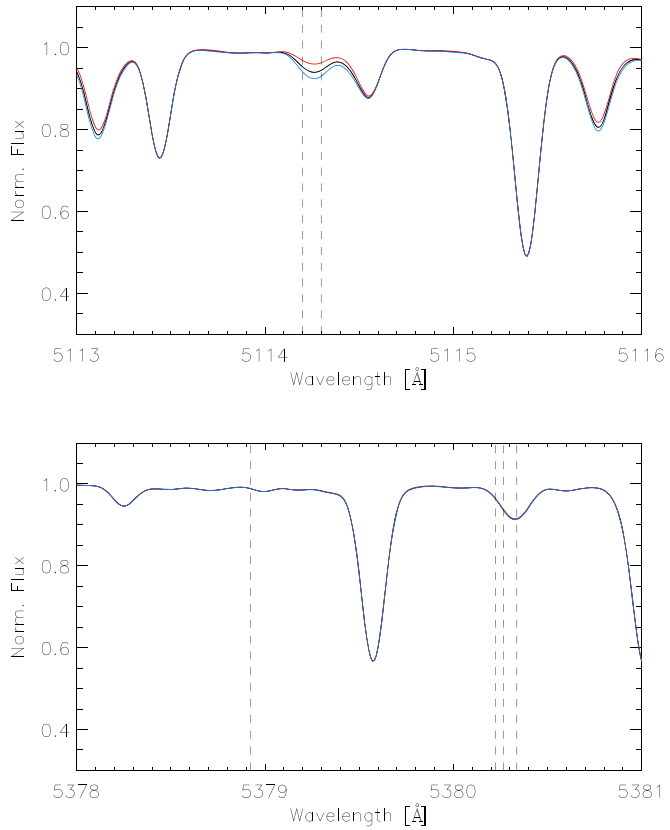


**Figure 5.** Comparison between the three synthetic spectra computed for the star 09473303-1018485 by using the same [C/Fe] = −0.21 and three different [O/Fe] values, namely, [O/Fe] = −0.4 (blue line), 0.0 (black line), and +0.4 (red line). The top panel shows a region with two strong $C_2$ lines (whose positions are indicated by the vertical dashed lines); the bottom panel shows one of the five regions containing the C I lines used to derive [C/Fe] (the vertical dashed lines indicate the positions of the four C I lines listed in Table 1).

component. Out of the several approaches adopted in the literature for identifying thin- and thick-disk stars, the two most used are those based on purely a chemical or a kinematical approach even if combinations of kinematics, metallicities, and stellar ages can also be adopted (see, e.g., Fuhrmann 1998).

### 3.1. Chemical Selection

Among several methods proposed so far to differentiate the Galactic disks, the ones based on stellar abundances have extensively been considered robust, mainly because chemistry is a relatively stable property of stars (Adibekyan et al. 2013, and references therein). Following such an approach, we use the position of the stars in the [Mg/Fe]–[Fe/H] plane to discriminate those belonging to the two different disks. Our analysis differs from the one by Adibekyan et al. (2013) since we used Mg, as in Kordopatis et al. (2015), instead of an average of the abundances of $\alpha$-elements (i.e., Mg, Si, and Ti). Our choice is based on the fact that the different $\alpha$-elements are produced by different stellar progenitors. In particular, Si and Ti are produced also by Type Ia supernovae, whereas Mg is not (Cescutti et al. 2007; Romano et al. 2010). Figure 6 shows the separation plot we adopted. The separation line (dashed green line) is somewhat arbitrary and was obtained in analogy with those used in Adibekyan et al. (2011, 2013) and Haywood et al. (2013).

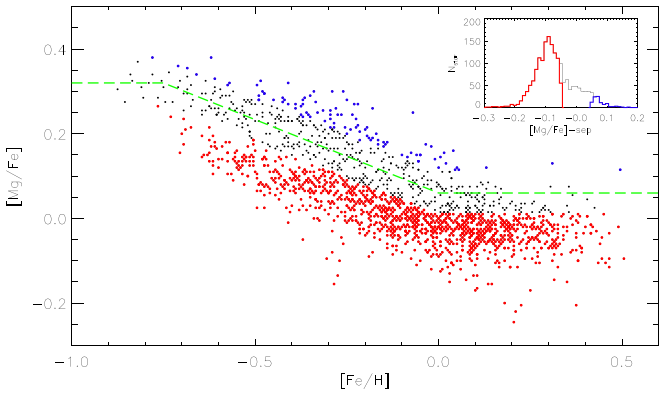


**Figure 6.** [Mg/Fe]–[Fe/H] diagram used to chemically select thin-disk (red points) and thick-disk (blue points) stars (see the text); stars falling in the avoidance region (see Section 3.1) are indicated by black points. In the upper right corner we show the distributions of [Mg/Fe] after subtracting the separation line (dashed green line in the main plot).

We classify as thick-disk stars (blue points) those above the separation line and as thin-disk stars (red points) those below. To minimize contamination, we adopted an avoidance region of ±0.05 dex. In this way, we obtained two samples of 1267 thin-disk stars ($\text{Thin}^{\text{C}}$ sample, where the superscript "C" indicates that it was obtained via a chemical selection) and 99 thick-disk stars ($\text{Thick}^{\text{C}}$ sample). In the upper right corner of Figure 6 we show the distributions of [Mg/Fe] after subtracting the separation line for all the stars (in green) and for the two samples (in red and in blue). The average 3D-NLTE corrections for the $\text{Thin}^{\text{C}}$ and $\text{Thick}^{\text{C}}$ samples are $-0.02 \pm 0.02$ dex and $-0.03 \pm 0.01$ dex, respectively.

### 3.2. Kinematical Selection

Among the different criteria to separate thin- and thick-disk populations using kinematical properties of the stars, a popular strategy is based on the assumption of Gaussian velocity distributions in each Galactic component (Bensby et al. 2003, 2014):

$$f(U, V, W) = k \cdot \exp\left(-\frac{(U_{\text{LSR}} - U_{\text{asym}})^2}{2\sigma_U^2} - \frac{(V_{\text{LSR}} - V_{\text{asym}})^2}{2\sigma_V^2} - \frac{W_{\text{LSR}}^2}{2\sigma_W^2}\right), \quad (1)$$

where

$$k = \frac{1}{(2\pi)^{2/3}\sigma_U \sigma_V \sigma_W}$$

normalizes the expression; $U_{\text{LSR}}$, $V_{\text{LSR}}$, and $W_{\text{LSR}}$ are the Galactic velocities of the stars in the local standard of rest (LSR); $\sigma_U$, $\sigma_V$, and $\sigma_W$ are the characteristic velocity dispersions for the different populations; and $U_{\text{asym}}$ and $V_{\text{asym}}$ are the asymmetric drifts. For a given star, when computing the likelihoods of belonging to one of the Galactic populations (i.e., $P_{\text{Thin}}$, $P_{\text{Thick}}$, $P_{\text{Halo}}$, $P_{\text{Hercules}}$), one has to take into account the local number densities of each population ($X_{\text{Thin}}$, $X_{\text{Thick}}$,

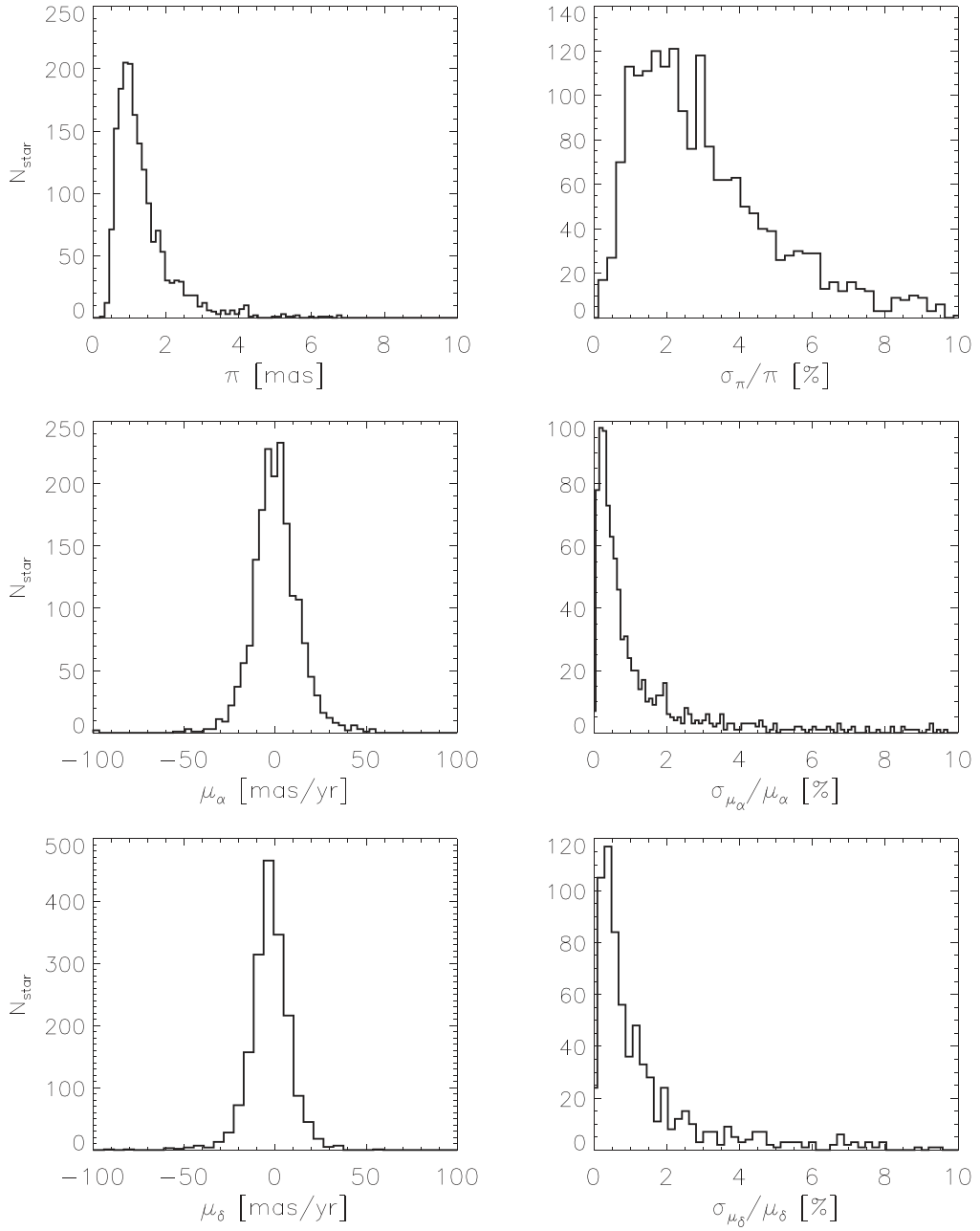


**Figure 7.** Distributions of $\pi$, $\mu_\alpha$, and $\mu_\delta$ (left panels) and their relative uncertainties (right panels) of the 1804 stars for which Galactic velocities are computed. Stars with large parallaxes (18 stars with $\pi > 10$ mas) or large proper motions (10 stars with $|\mu_\alpha| > 100$ mas yr$^{-1}$ and 8 stars with $|\mu_\delta| > 100$ mas yr$^{-1}$) were excluded from the figures to increase readability.

$X_{\rm Halo}$, $X_{\rm Hercules}$):

$$\begin{aligned} P_{\rm Thin} &= X_{\rm Thin} \cdot f_{\rm Thin} \\ P_{\rm Thick} &= X_{\rm Thick} \cdot f_{\rm Thick} \\ P_{\rm Halo} &= X_{\rm Halo} \cdot f_{\rm Halo} \\ P_{\rm Hercules} &= X_{\rm Hercules} \cdot f_{\rm Hercules}, \end{aligned} \quad (2)$$

where the subscript "Hercules" refers to the Hercules stream (Fux 2001).

The values for the velocity dispersions, asymmetric drifts, and observed fractions ($X$) of each population in the solar neighborhood are given in Bensby et al. (2014, Table A.1).

A shortcoming of this approach is that the assumption of Gaussian distributions is valid only as a first-order approximation (Binney 2010). However, since there is no clear consensus in the literature on the actual shape of the velocity distributions, we used, for our purposes, normal distributions, as also done in several recent papers (e.g., Buder et al. 2019).

#### 3.2.1. Space Velocities and Selection Criteria

In order to calculate space velocities ($U_{\rm LSR}$, $V_{\rm LSR}$, and $W_{\rm LSR}$) for our sample stars, we need distances (or parallaxes, $\pi$), proper motions ($\mu_\alpha$, $\mu_\delta$), and radial velocities ($V_{\rm r}$). We searched for $\pi$, $\mu_\alpha$, and $\mu_\delta$ in the second *Gaia* data release (Gaia DR2; Gaia Collaboration et al. 2018), while for $V_{\rm r}$ we used GES iDR5 values with typical percentage error below 7%. For each star of our UVES–U580 sample we made a cross-match between the GES and *Gaia* DR2 coordinates by using the

*gaiadr2.gaia_source* table and a match radius of 1″. Each GES iDR5 star, if detected, was associated with the nearest *Gaia* DR2 source, leading to a sample of 2113 stars. Out of these stars, we accepted only those characterized by small relative errors (less than 10%) in $\pi$, $\mu_\alpha$, and $\mu_\delta$, thus obtaining an astrometric sample of 1804 dwarf stars suitable for computing accurate Galactic velocities. Figure 7 shows the distributions of parallaxes (top left panel), R.A. (middle left panel) and decl. (bottom left panel) proper motions, and their percentage errors (right panels) for the 1804 stars. As can be seen, the distributions of the relative errors in $\pi$, $\mu_\alpha$, and $\mu_\delta$ are peaked at about 2%, 0.2%, and 0.4%, respectively.

Starting from the obtained $\pi$, $\mu_\alpha$, $\mu_\delta$, and $V_r$ values, we computed the Galactic radii, $R$, the distance from the Galactic plane, $z$, and the velocities $U_{\rm LSR}$, $V_{\rm LSR}$, and $W_{\rm LSR}$, together with their uncertainties, $\Delta_U$, $\Delta_V$, $\Delta_W$, using a program kindly provided by R. Fiorentin (2019, private communication). The program assumes that the Sun is 8.2 kpc away from the Milky Way center, the LSR is rotating at 232 km s$^{-1}$ around the Galactic center (McMillan 2017a, 2017b), and the LSR peculiar velocity components of the Sun are $(U_\odot, V_\odot, W_\odot) = (-11.1, 12.24, 7.25)$ km s$^{-1}$ (Schönrich et al. 2010) in a right-handed coordinate system. Figure 8 shows the Galactic positions of our stars; most of the stars have $R$ between 6.5 and 8.5 kpc and $z$ between −2.0 and 1.5 kpc.

From $U_{\rm LSR}$, $V_{\rm LSR}$, and $W_{\rm LSR}$ and their uncertainties we computed, using Equations (1) and (2), the probabilities $P_{\rm Thin}$, $P_{\rm Thick}$, $P_{\rm Halo}$, $P_{\rm Hercules}$ and their uncertainties $\sigma_{P_{\rm Thin}}$, $\sigma_{P_{\rm Thick}}$, $\sigma_{P_{\rm Halo}}$, $\sigma_{P_{\rm Hercules}}$. In computing both $\Delta_U$, $\Delta_V$, $\Delta_W$ and $\sigma_{P_{\rm Thin}}$, $\sigma_{P_{\rm Thick}}$, $\sigma_{P_{\rm Halo}}$, $\sigma_{P_{\rm Hercules}}$ we did not apply the standard error propagation, but we used the proper covariance matrices owing to the fact that the variables are correlated.

We then define a sample of 1356 stars as representative of the thin-disk population (hereafter called the Thin$^{\rm K}$ sample, where the superscript "K" indicates that it was obtained via a kinematical selection) by using the following criteria:

$$\begin{aligned} P_{\rm Thin} - \sigma_{P_{\rm Thin}} &> 2(P_{\rm Thick} + \sigma_{P_{\rm Thick}}) \\ &> 2(P_{\rm Halo} + \sigma_{P_{\rm Halo}}) \\ &> 2(P_{\rm Hercules} + \sigma_{P_{\rm Hercules}}). \end{aligned} \quad (3)$$

In analogy we define a sample of 196 stars as representative of the thick-disk population (Thick$^{\rm K}$ sample) by using the following criteria:

$$\begin{aligned} P_{\rm Thick} - \sigma_{P_{\rm Thick}} &> 2(P_{\rm Thin} + \sigma_{P_{\rm Thin}}) \\ &> 2(P_{\rm Halo} + \sigma_{P_{\rm Halo}}) \\ &> 2(P_{\rm Hercules} + \sigma_{P_{\rm Hercules}}). \end{aligned} \quad (4)$$

Adopting a similar criterion, we found that six stars of our sample belong to the halo and four stars belong to the Hercules stream. The factor of 2 in Equations (3) and (4) is introduced to minimize the contamination between the two samples. It must be noticed that our selection criteria are more robust than those adopted in general by other authors, such as Bensby et al. (2014), since we take into account also the uncertainties on the $P$ probabilities due to the $\Delta_U$, $\Delta_V$, $\Delta_W$ values. The average 3D-NLTE corrections for the Thin$^{\rm K}$ and Thick$^{\rm K}$ samples are $-0.02 \pm 0.02$ dex and $-0.03 \pm 0.01$ dex, respectively.

### 3.3. Sample Selection on the Basis of Orbital Parameters

In the previous section we discriminated between thin- and thick-disk stars by using the present stellar Galactic velocities.

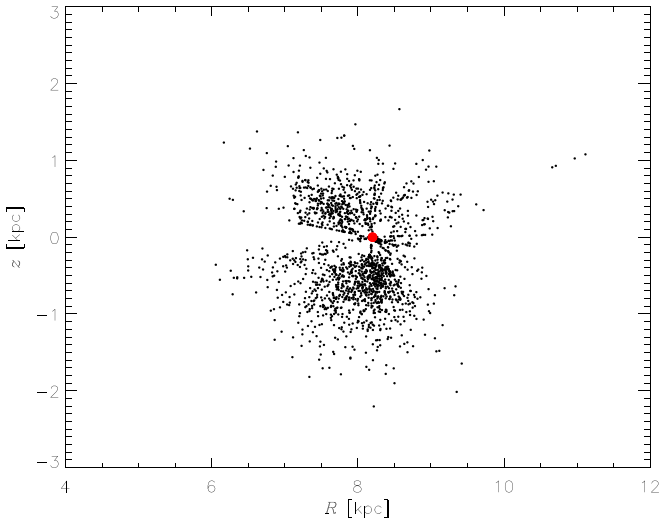


**Figure 8.** Galactic radii and vertical distances from the Galactic plane for the sample of 1804 stars with accurate $\pi$, $\mu_\alpha$, and $\mu_\delta$; the red filled circle shows the Sun position.

Obviously, the stars during their life change position and velocity owing to their motion in the Galaxy. In order to take into account this fact, we compute stellar Galactic orbits for the 1804 stars with known distances and Galactic velocities. Orbital parameters for each star (maximum and minimum galactocentric radii, $R_{\rm max}$ and $R_{\rm min}$, maximum absolute distance from Galactic plane, $|Z_{\rm max}|$, and orbital eccentricity, $\epsilon$) were calculated using a code kindly provided to us by J. P. Fulbright (private communication). The code uses an integrator developed by D. Lin first used in Fulbright (2002) and assumes a three-component potential (halo, disk, and bulge) based on the potential described in Johnston et al. (1996) and Johnston (1998). Each star is followed for 15 Gyr, at a step of 3 Myr. It is well known that stellar migration, via churning and blurring, makes it difficult to estimate the birth radius of each star, and therefore its identification with $R_{\rm med} = 0.5 \times (R_{\rm min} + R_{\rm max})$ is not straightforward. In particular, we do not have in our Galactic potential deviations from axisymmetry like those introduced by the bar and the spiral arms. Therefore, we will use in the following only $|Z_{\rm max}|$ and $\epsilon$, which we assume, in a first approximation, are not significantly affected by stellar migration.

To select the Thin$^{\rm O}$ and Thick$^{\rm O}$ samples, we used the plane $\epsilon$ versus $|Z_{\rm max}|$. We fix an upper limit for the $|Z_{\rm max}|$ of the thin-disk stars at 0.80 kpc, which is the value where the stellar densities of the two disks, computed using the thin- and thick-disk model of Widrow et al. (2012) with scale heights $H_1$ and $H_2$ from Ferguson et al. (2017), are equal. Then, to remove the contamination of thick-disk stars with low $|Z_{\rm max}|$, we require also an eccentricity lower than 0.2 (see discussion in Wilson et al. 2011). For the thick-disk star selection, we require $0.8\ {\rm kpc} < |Z_{\rm max}| < 2.0\ {\rm kpc}$ and $0.3 < \epsilon < 0.7$, where the upper values are needed to exclude any halo star. With such criteria we obtain two samples, Thin$^{\rm O}$ and Thick$^{\rm O}$ (see Figure 9), containing 934 and 90 thin- and thick-disk stars with average 3D-NLTE corrections of $-0.02 \pm 0.02$ dex and $-0.03 \pm 0.01$ dex, respectively.

The comparison of the kinematical and chemical properties of the three pairs of thin- and thick-disk samples is presented in the following sections, while the percentages of stars in common between the different selections are given in Section 7.

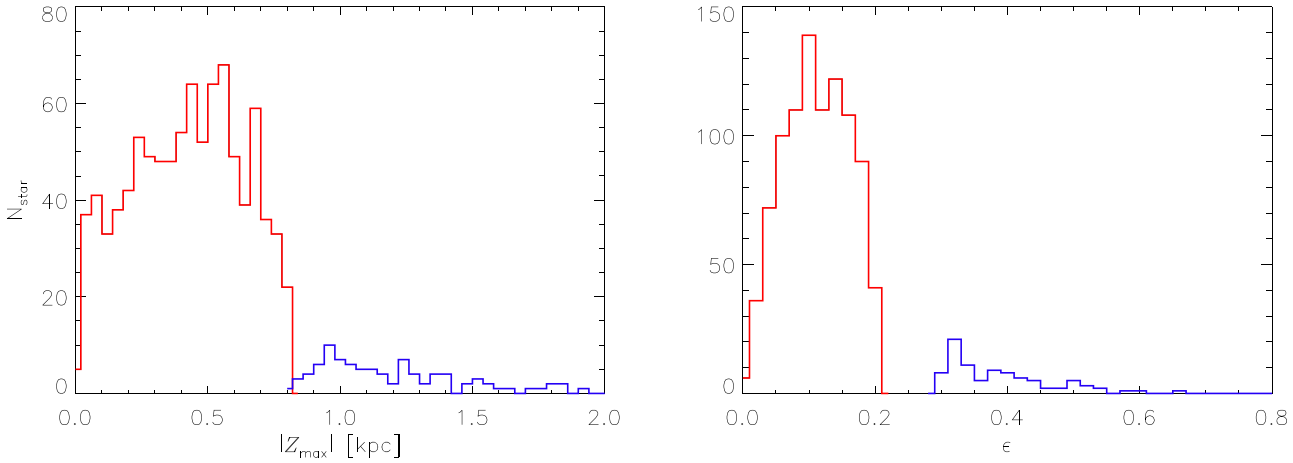


**Figure 9.** Distributions of $|Z_{\rm max}|$ and eccentricity, $\epsilon$, for Thin$^{\rm O}$ (red) and Thick$^{\rm O}$ (blue) samples.

## 4. Kinematical Properties of the Thin- and Thick-disk Star Samples

To study the kinematical properties of the different Galactic populations, a commonly used tool is the Toomre diagram, which is a representation of the combined vertical and radial kinetic energies versus the rotational energy. As a first approximation, the low-velocity stars, with a total velocity $v_{\rm tot} \equiv (U_{\rm LSR}^2 + V_{\rm LSR}^2 + W_{\rm LSR}^2)^{1/2}$ less than 50 km s$^{-1}$, are mainly thin-disk stars, while the stars with 70 km s$^{-1}$ $\leqslant v_{\rm tot} \leqslant$ 180 km s$^{-1}$ are likely to be thick-disk stars (e.g., Nissen 2004). Moreover, the thick disk is as a whole a more slowly rotating stellar system than the thin disk, lagging behind the LSR by approximately 50 km s$^{-1}$ (e.g., Soubiran et al. 2003). The Galactic velocity dispersions ($\sigma_U$, $\sigma_V$, $\sigma_W$) are also larger in the thick disk than in the thin disk. For example, Soubiran et al. (2003) found ($\sigma_U$, $\sigma_V$, $\sigma_W = 39 \pm 2$ km s$^{-1}$, $20 \pm 2$ km s$^{-1}$, $20 \pm 1$ km s$^{-1}$) and ($\sigma_U$, $\sigma_V$, $\sigma_W = 63 \pm 6$ km s$^{-1}$, $39 \pm 4$ km s$^{-1}$, $39 \pm 4$ km s$^{-1}$) for the thin and thick disks, respectively, in reasonable agreement with the values by Bensby et al. (2014) ($\sigma_U$, $\sigma_V$, $\sigma_W = 35$, 20, 16 km s$^{-1}$, $\sigma_U$, $\sigma_V$, $\sigma_W = 67$, 38, 35 km s$^{-1}$) used in Section 3.2.1.

In the three left panels of Figure 10 we show the positions in the Toomre diagram of the stars we attribute to thin or thick disks by using the different selection criteria described in Sections 3.1–3.3. As can be seen, stars belonging to the thin-disk samples and those belonging to the thick-disk samples are fairly kinematically separated. The separation is less clear in the top panel, which refers to the chemical selection. It is worthwhile noticing that this selection does not take into account any kinematical stellar property. Note also that we do not have *Gaia* DR2 data for all the Thin$^{\rm C}$ and Thick$^{\rm C}$ stars, and thus the corresponding Toomre diagram and histograms contain only 1065 and 92 thin- and thick-disk stars, respectively, instead of 1267 and 99. As far as the other two selections are concerned, while the separation in the middle panel is expected since the kinematical selection is actually based on the stellar Galactic velocities, the clear segregation in the bottom panel is less predictable even if not completely unexpected. In the three selection cases there is always a common interval in the $v_{\rm tot}$ distributions (right panels) of the two samples with a decreasing overlap going from top to bottom. The widest overlap is obtained in the region 0 km s$^{-1}$ $< v_{\rm tot} \lesssim$ 130 km s$^{-1}$ when using the chemical selection; the overlap region is 70 km s$^{-1}$ $\lesssim v_{\rm tot} \lesssim$ 100 km s$^{-1}$ for the kinematical selection and reduces to 70 km s$^{-1}$ $\lesssim v_{\rm tot} \lesssim$ 90 km s$^{-1}$ for orbital selection. It is also worthwhile mentioning that the difference between the mean rotational velocity of the two samples ($\langle V_{\rm thin} \rangle - \langle V_{\rm thick} \rangle$) is 36, 50, and 55 km s$^{-1}$ for the chemical, kinematical, and orbital selection, respectively. In Table 2 we report the dispersion velocities of the different samples, ($\sigma_U^{\rm C}$, $\sigma_V^{\rm C}$, $\sigma_W^{\rm C}$), ($\sigma_U^{\rm K}$, $\sigma_V^{\rm K}$, $\sigma_W^{\rm K}$), and ($\sigma_U^{\rm O}$, $\sigma_V^{\rm O}$, $\sigma_W^{\rm O}$); independently of the adopted selection, the thick-disk stars show always larger dispersion velocities than the thin-disk ones, as expected (see, e.g., Soubiran et al. 2003; Bensby et al. 2014).

## 5. Chemical Properties of the Thin- and Thick-disk Star Samples

The left panels of Figure 11 show the [C/H] versus [Fe/H] for the thin- and thick-disk samples. As can be seen, and evidenced by the regression lines, thick-disk stars have larger C abundance than thin-disk stars at the same [Fe/H] on average. The regression lines have slopes that differ by less than $2\sigma$; therefore, the slope differences may not be significant. In the right panels we show the normalized generalized distributions of [C/Fe] built by summing individual unit area Gaussians computed for each star, in the proper sample, by using its [C/Fe] value and uncertainty and then normalizing the results to the number of objects. The thin-disk sample (red) distribution is, for any kind of selection, peaked at lower [C/Fe] than the thick-disk sample distribution (blue). A two-sided Kolmogorov–Smirnov test, performed using the "kstwo" IDL[25] routine, confirms that the two cumulative distribution functions are significantly different for all three different selection methodologies adopted (prob always less than 1.E-8). The left panels show for both the thin- and thick-disk stars a large scatter in the [C/H] values. Such a scatter was also found by Nissen & Gustafsson (2018) and Amarsi et al. (2019c), and they suggested that it can be explained by variations in the dust-to-gas ratio in different star-forming gas clouds and/or by the need to apply differential 3D-NLTE corrections to 1D-LTE abundances (see discussion at the end of Section 2.2.2).

To better understand the behavior of [C/Fe], we plotted in Figure 12 the trends of [C/Fe] versus [Fe/H] for the thin- and thick-disk samples for the three different selections. In order to

[25] Interactive Data Language: https://www.harrisgeospatial.com/Software-Technology/IDL.

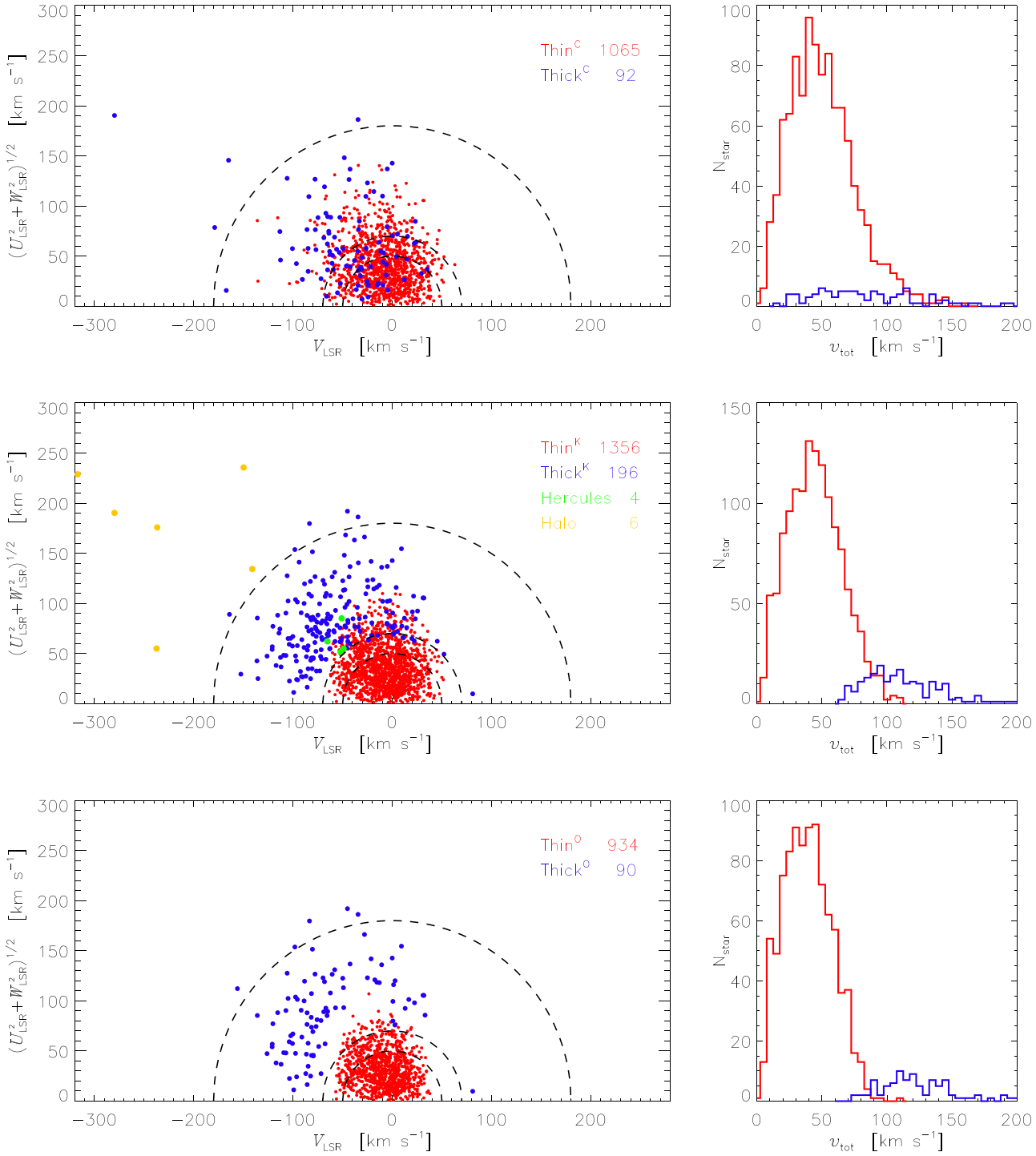


**Figure 10.** Toomre diagrams for the thin-disk (red points) and thick-disk (blue points) stars with different selections. Dotted lines show constant values of the total space velocity, $v_{tot} \equiv (U^2_{LSR} + V^2_{LSR} + W^2_{LSR})^{1/2}$ at 50, 70, and 180 km s$^{-1}$ i.e., the thresholds used by Nissen (2004) to separate, as a first approximation, thin- and thick-disk stars (see Section 4). Top panels: vertical and radial kinetic energy versus rotational ones (left panel) and distribution of total velocities for stars belonging to Thin$^C$ and Thick$^C$ samples with available Galactic velocities. Middle panels: same as the top panels, but for Thin$^K$ and Thick$^K$ samples; stars belonging to the Hercules stream (green points) and the halo (yellow points) are also indicated in the left panel. Bottom panels: same as the top panels, but for Thin$^O$ and Thick$^O$ samples.

get rid of the quite large scatter in the data shown in Figure 11, we opted to plot, instead of the individual values, the mean ones in partially overlapped bins by using a running average (using a fixed number of points), together with, for each bin, their standard deviations. As can be seen, for all the selections, the thick-disk stars show a higher [C/Fe] than the thin-disk stars for $-0.5 \lesssim$ [Fe/H] $\lesssim -0.1$. In the case of the chemical selection, the [Fe/H] range, for which the thick and thin trends are separated, extends to [Fe/H] $\simeq +0.1$, while, in the case of the kinematical selection, we have an intermediate situation between the other two cases. The so-obtained [C/Fe] versus [Fe/H] trends recall the behavior of $\alpha$-elements versus [Fe/H] but with a less pronounced separation. It is worth noticing that in all the panels the thin-disk sequences at [Fe/H] $= 0$ fall below the zero horizontal line. This offset was also found in other literature works (e.g., Shi et al. 2002; Nissen et al. 2014;

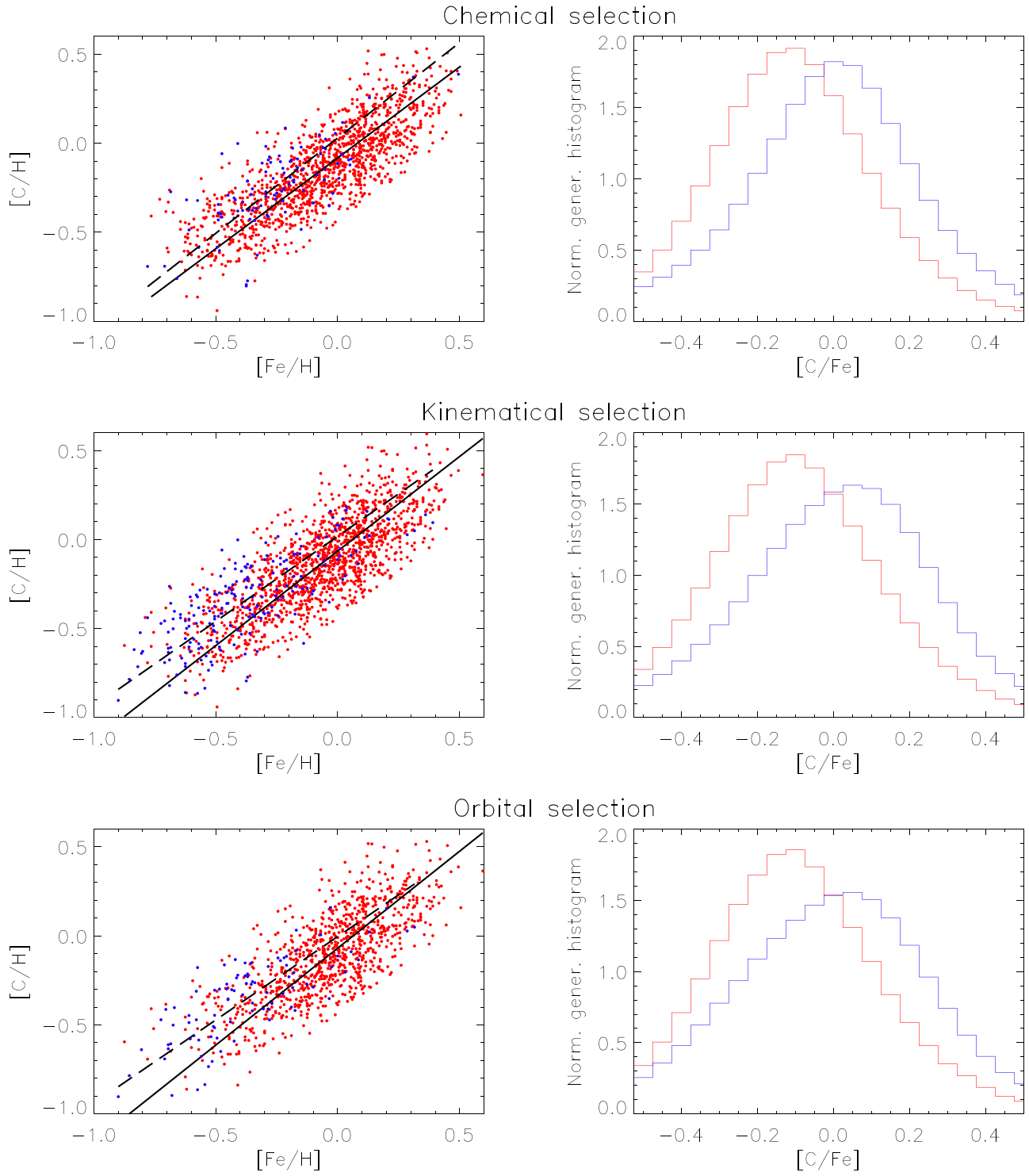


**Figure 11.** [C/H]–[Fe/H] diagrams (left panels) and [C/Fe] normalized generalized histograms (right panels) for thin-disk (red) and thick-disk (blue) samples. Top panels: $\text{Thin}^{\text{C}}$ and $\text{Thick}^{\text{C}}$ samples; middle panels: $\text{Thin}^{\text{K}}$ and $\text{Thick}^{\text{K}}$ samples; bottom panels: $\text{Thin}^{\text{O}}$ and $\text{Thick}^{\text{O}}$ samples. Regression lines for thin (solid) and thick (dashed) samples are superimposed on the left panels.

Nissen & Gustafsson 2018) and suggests that, maybe, the Sun can be carbon-rich with respect to the average thin disk (see also Figure 2 in Meléndez et al. 2009).

Our results are in agreement with those by Reddy et al. (2006), Delgado Mena et al. (2010), Nissen et al. (2014), and Suárez-Andrés et al. (2017). In particular, on the basis of a kinematical selection, Reddy et al. (2006) found that the abundance ratios [C/Fe] for their thick-disk sample stars with [Fe/H] $< -0.4$ were, on average, larger than for their thin-disk stars of the same [Fe/H]. They also stated that carbon behaves like Mg and other $\alpha$-elements. Nissen et al. (2014), by also implementing a kinematical selection for some stars and a chemical one for other stars, found that their thin-disk stars fall below the thick-disk ones in the [C/Fe] versus [Fe/H] diagram for [Fe/H] $\sim -0.3$ and suggested that the two populations merge at higher metallicities. On the other hand, our results

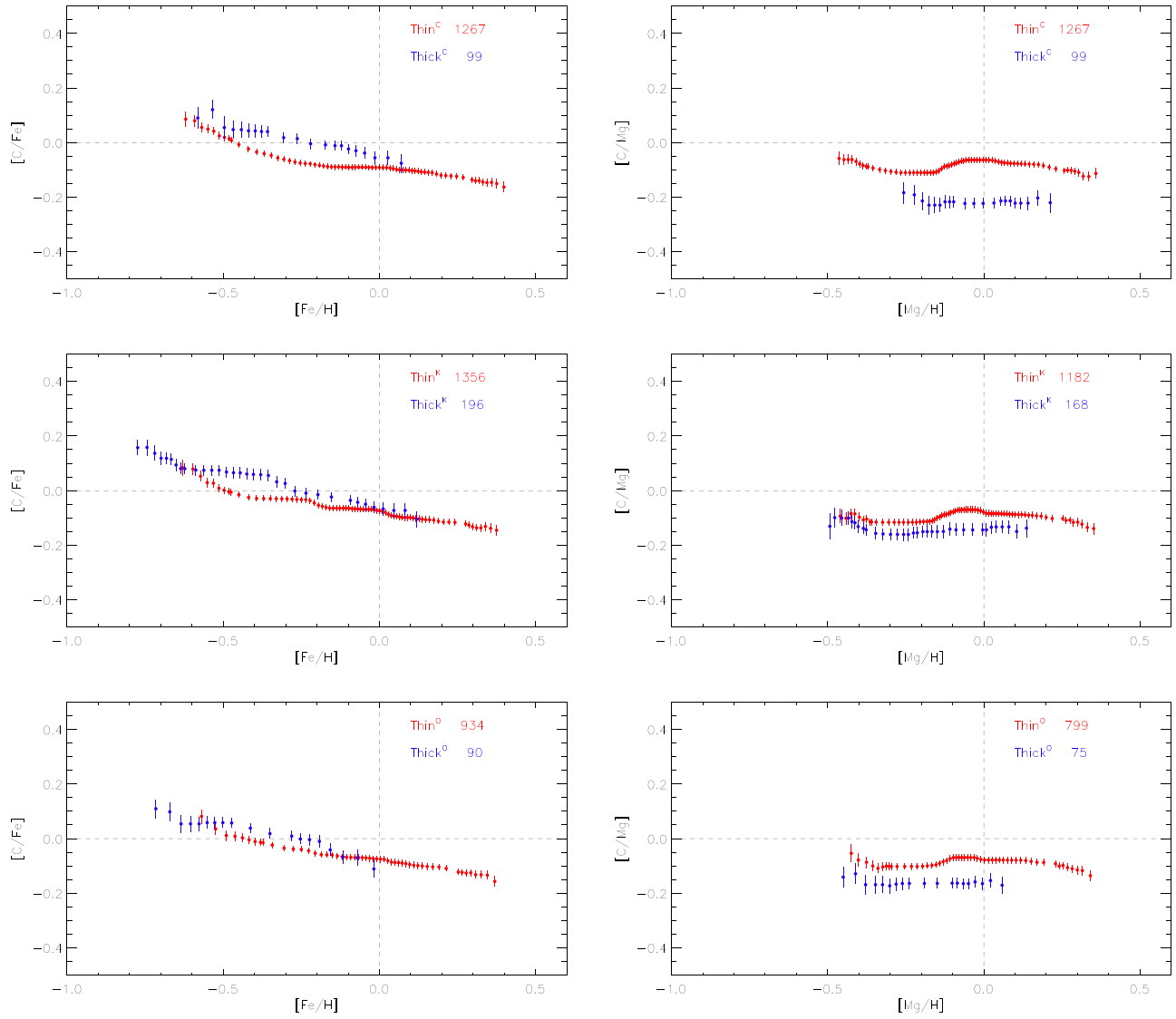


**Figure 12.** [C/Fe]–[Fe/H] diagrams (left panels) and [C/Mg]–[Mg/H] diagrams (right panels) for thin-disk (red) and thick-disk (blue) samples; binned running averages and standard deviations are plotted. Top panels: Thin$^{C}$ and Thick$^{C}$ samples; middle panels: Thin$^{K}$ and Thick$^{K}$ samples; bottom panels: Thin$^{O}$ and Thick$^{O}$ samples.

contradict those by Bensby & Feltzing (2006), who, by using a kinematical selection, found that the [C/Fe] versus [Fe/H] trends for the thin and thick disks are totally merged and flat for subsolar metallicities, with a shallow decline for the thin-disk stars from [Fe/H] $\simeq 0$ up to [Fe/H] $\simeq +0.4$. On the contrary, our data show a general decrease of [C/Fe] for both thin- and thick-disk stars, with increasing [Fe/H] values even if the top and middle left panels seem to indicate a flattening for the thin-disk stars with $-0.5 \lesssim$ [Fe/H] $\lesssim 0$.

In order to study the origin and Galactic evolution of carbon, the [C/O]–[O/H] diagram is often used in the literature. In fact, since oxygen is exclusively produced in massive stars on a relatively short timescale, the change in [C/O] as a function of [O/H] gives hints on the yields and timescales of carbon production in different types of stars (see Cescutti et al. 2009, and references therein). Nevertheless, the derivation of oxygen abundances for dwarf stars within GES iDR5 has not yet been completed, (for giants, see Magrini et al. 2018); therefore, we decided to use magnesium instead of oxygen. The right panels of Figure 12 show the trends of [C/Mg] versus [Mg/H] for the thin- and thick-disk samples for the three different selections. As can be seen, for all the selections, the thin-disk stars show a higher [C/Mg] than the thick-disk stars for the same [Mg/H]. In the case of the chemical selection, the difference in [C/Mg] is probably enhanced by the fact that the thick- and thin-disk stars are actually high- and low-Mg stars. On the other hand, the presence of a separation also in the other selection cases indicates that there is an excess of [C/Mg] in the thin-disk stars with respect to the thick disk. All the panels show almost flat trends, confirming the similarity of the C and $\alpha$-element behaviors suggested by the left panels of Figure 12.

## 6. Ages of the Thin- and Thick-disk Star Samples

A better understanding of carbon evolution in our Galaxy could be achieved by determining the ages of the stars in our sample. However, the ages of stars cannot be directly measured, and their determination, in particular for field stars, is indeed very difficult (see, e.g., Randich et al. 2018, and references therein). A number of methods have been devised to

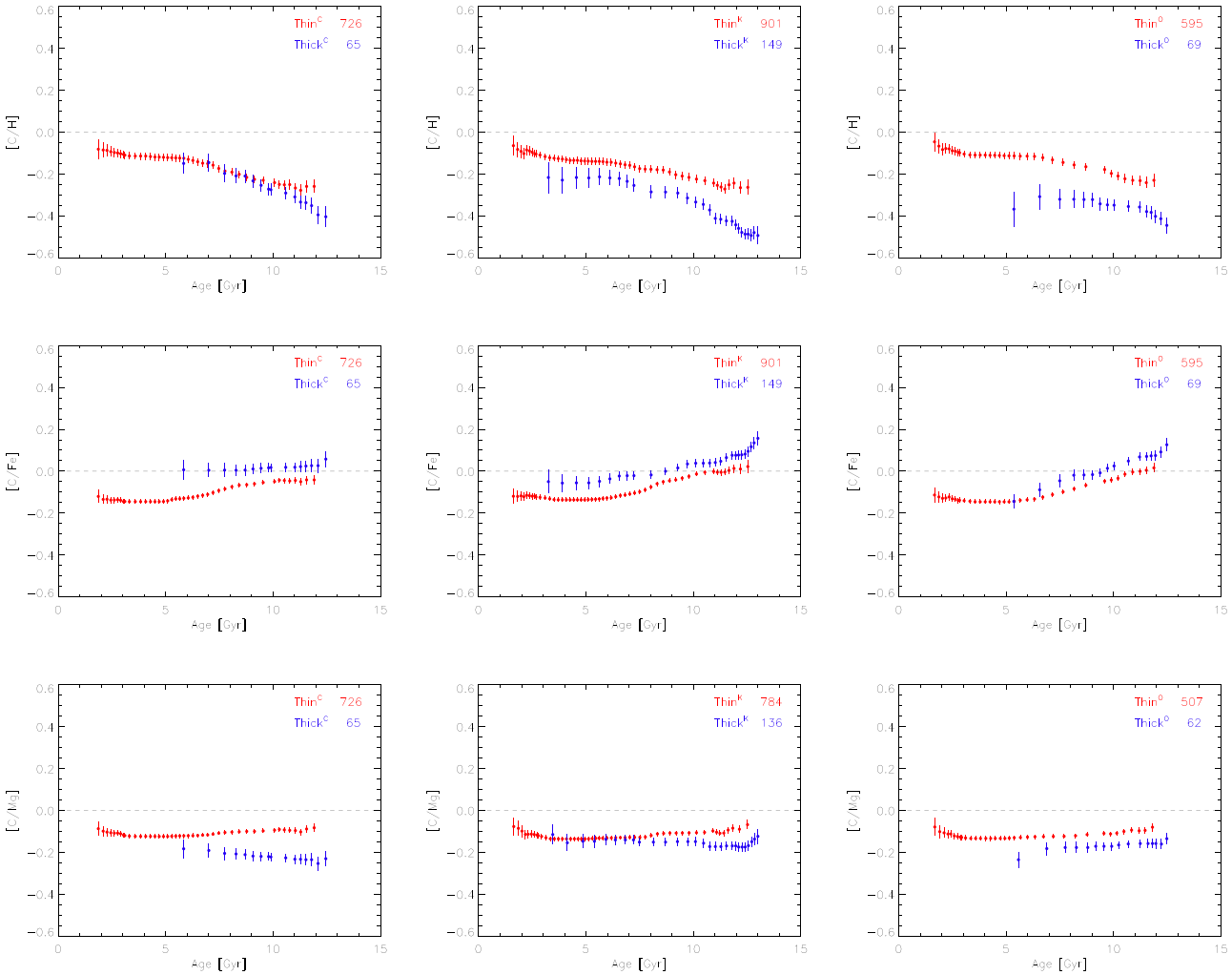


**Figure 13.** [C/H] (top panels), [C/Fe] (middle panels), and [C/Mg] (bottom panels) vs. age diagrams for thin-disk (red) and thick-disk (blue) samples. Left panels: $\mathrm{Thin}^{\mathrm{C}}$ and $\mathrm{Thick}^{\mathrm{C}}$ samples; middle panels: $\mathrm{Thin}^{\mathrm{K}}$ and $\mathrm{Thick}^{\mathrm{K}}$ samples; right panels: $\mathrm{Thin}^{\mathrm{O}}$ and $\mathrm{Thick}^{\mathrm{O}}$ samples.

derive stellar ages. While gyrochronology and asteroseismology (or combinations of them) are recognized as the most reliable processes for dating stars (Soderblom 2010; Angus et al. 2019), such methods are not yet applicable to our stellar sample since it is composed of field stars that still lack oscillation data. We implement an isochrone comparison Bayesian approach, as first proposed by Pont & Eyer (2004) and Jørgensen & Lindegren (2005), of a commonly used technique that is based on the comparison between observational quantities (e.g., magnitudes) and derived parameters (like effective temperatures) that has been extensively applied in the literature (see, e.g., Casagrande et al. 2011; Haywood et al. 2013; Bensby et al. 2017; Howes et al. 2019). On the basis of previous works, it has been demonstrated that even small uncertainties on $T_{\mathrm{eff}}$ values and magnitudes can result in large age errors; hence, our approach aims at deriving relative ages to provide valuable insights on the overall age characteristics of our stellar samples.

In this paper we use a program kindly provided to us by L. Lindegren (2019, private communication) based on the Bayesian age estimation code first described by Jørgensen & Lindegren (2005), assuming a flat metallicity prior due to the good precision of GES estimates (see discussion in Jørgensen & Lindegren 2005). The program, which uses Padova isochrones, was modified by us in order to be able to use as input data the *Gaia* G magnitude by adopting the color–color transformations by Evans et al. (2018). The absolute G magnitudes of our stars, computed from *Gaia* DR2 parallaxes and corrected for reddening by using the 3D Galactic extinction model by Drimmel et al. (2003), and the GES iDR5 $T_{\mathrm{eff}}$ values were given in input to our program. In such a way we obtain an age estimate, together with the FWHM of its probability distribution ($\mathrm{FWHM}_{\mathrm{Age}}$), for 1751 stars (53 stars have absolute magnitudes outside the range of our isochrone database). Then, to remove the most uncertain ages, we discarded those stars (518) with $\mathrm{FWHM}_{\mathrm{Age}} > 8$ Gyr that correspond to low main-sequence stars where isochrones are overlapping, thus affecting the accuracy of age determinations. It is worth noticing that also the absolute individual ages of the remaining 1098 stars may still have quite large uncertainties due to systematic errors and inaccuracies in the input data of the adopted Bayesian method and in the input physics of the isochrones. In order to cope with this problem, we adopted the same technique used in Section 5 to get rid of the scatter, i.e., we computed mean ages and their standard deviations in bins built by using a running average. Figures 13 and 14 show the trends of [C/H], [C/Fe], [C/Mg], $R_{\mathrm{med}}$, and $|Z_{\mathrm{max}}|$ versus age for the thin-disk (red) and

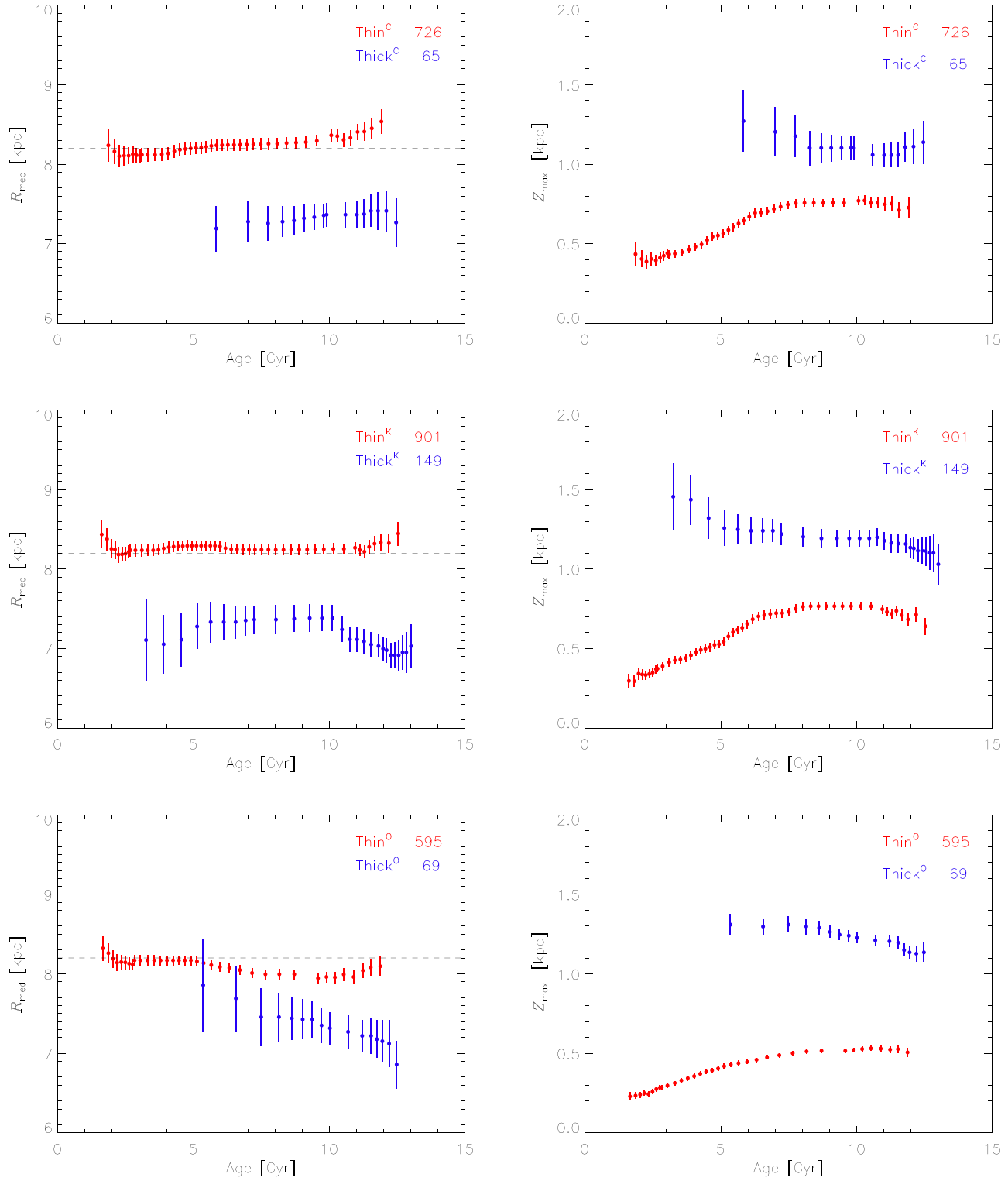


**Figure 14.** $R_{med}$ (left panels) and $|Z_{max}|$ vs. age diagrams for thin-disk (red) and thick-disk (blue) samples. Top panels: Thin$^C$ and Thick$^C$ samples; middle panels: Thin$^K$ and Thick$^K$ samples; bottom panels: Thin$^O$ and Thick$^O$ samples.

thick-disk (blue) samples selected chemically, kinematically, and using orbit characteristics.

The content of Figures 13 and 14 can be summarized as follows:

1. All the panels show, for any of the three selections, i.e., for each pair of samples, that the thick-disk stars are, on average, older than the thin-disk ones (see also Figure 15, where the extended wings of the normalized generalized age histograms, built by summing the individual age probability distributions, at low ages for the thick-disk stars and at high ages for the thin-disk stars are probably spurious features due to the large uncertainties affecting individual stellar ages). This is in agreement with the

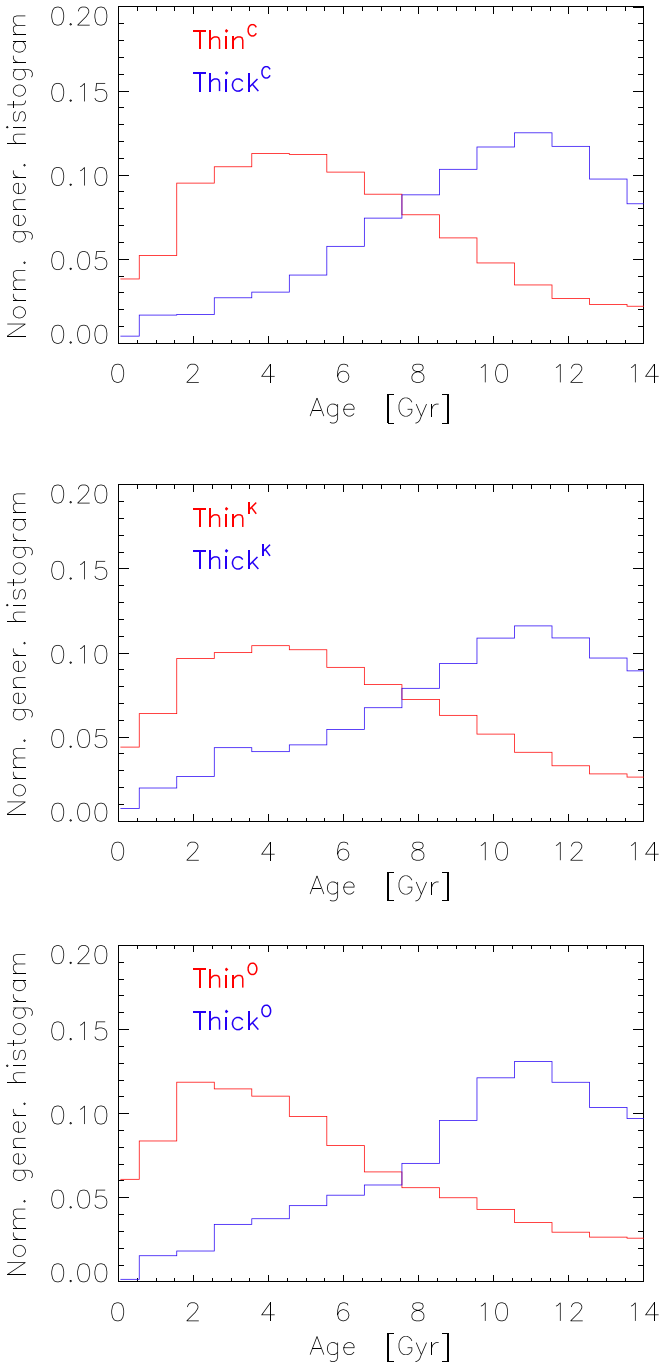


**Figure 15.** Normalized generalized age histograms for thin-disk (red) and thick-disk (blue) samples. Top panels: Thin$^C$ and Thick$^C$ samples; middle panels: Thin$^K$ and Thick$^K$ samples; bottom panels: Thin$^O$ and Thick$^O$ samples.

common understanding of GCE based on serial and two-infall models (Grisoni et al. 2017, and references therein), which predict that the thick disk formed before the thin one. Also in a cosmological context the formation of the thick and thin disks can be explained by means of an early and later accretion of gas, respectively (Calura & Menci 2009; Spitoni et al. 2019, and references therein), with a delay between two episodes that typically is of a few gigayears.

2. According to our results, thin-disk stars span an age range from ∼2 to ∼12 Gyr, which would indicate that the formation of the thin disk took place about 2–3 Gyr after the initial stages of the Milky Way evolution. This is in qualitative agreement with chemical abundance studies matched with asteroseismologic age determinations, which indicate a delay of ∼4 Gyr between the first and second accretion episodes that originated the Milky Way disk (Spitoni et al. 2019).
3. The thick-disk stars span an age range from ∼5 to ∼13 Gyr. Therefore, our results show hints that the thick disk started forming about 2 Gyr before the thin disk and that its formation lasted about 6–8 Gyr.
4. The oldest thick-disk stars have lower [C/H] than the thin-disk stars. This is more evident for the selection based on orbital parameters and less evident for the chemical selection. The trend with age shows a steeper increase for both the oldest and the youngest stars, suggesting that C is produced at the beginning by massive stars and in more recent times by low-mass stars or by high-metallicity massive stars owing to their enhanced mass loss. This is in agreement with the results of Nissen et al. (2014) and with the predictions of the "best-fitting model" by Carigi et al. (2005).
5. Thick-disk stars have higher [C/Fe] than thin-disk stars for all the selections. The thick-disk trends show a monotonic decrease of [C/Fe] with decreasing age. On the other hand, the thin-disk trends show a decrease with age from 10 to about 5 Gyr, a flattening from 5 to 3 Gyr, and then a hint of uprising for the youngest stars, suggesting again that there is an extra source of C at more recent times due to low-mass stars.
6. Both thin- and thick-disk stars show almost flat trends of [C/Mg] with age and an increase of the ratio for the youngest thin-disk stars. The average [C/Mg] difference between the two chemically selected samples is, to some extent, expected because of the choice of identifying thin- and thick-disk stars with high and low [Mg/Fe] stars, respectively. However, the increase of [C/Mg] for the youngest stars is plausible evidence that low-mass stars or massive stars at high metallicity owing to enhanced mass loss contribute a significant amount of C at recent times.
7. Thick-disk stars have, on average, lower $R_{\rm med}$ and higher $|Z_{\rm max}|$ than thin-disk stars.
   1. The thin-disk stars span an $R_{\rm med}$ range from ∼8.0 to ∼8.5 kpc, with an almost flat behavior.
   2. The thick-disk stars span an $R_{\rm med}$ range from ∼7 to ∼7.5 kpc, showing that the oldest stars were formed at smaller $R_{\rm med}$. These are the diagrams ($R_{\rm med}$ vs. age) that show the largest differences between the differently selected samples, in particular for the thick-disk stars, and are also the less reliable ones since stellar migration can prevent us from using our computed $R_{\rm med}$ values as indicators of the stellar birthplaces.
   3. The thin-disk stars span a $|Z_{\rm max}|$ range from ∼0.3 to ∼0.8 kpc (but for the sample selected using orbital parameters, which is confined below 0.6) with a trend of decreasing $|Z_{\rm max}|$ with decreasing age starting at ∼7 Gyr.
   4. The thick-disk stars span a $|Z_{\rm max}|$ range from ∼1.1 to ∼1.5 kpc. The trend with age is almost flat, with some hints of increasing $|Z_{\rm max}|$ for decreasing age. The larger separation in $|Z_{\rm max}|$ between the thin- and thick-

**Table 3**
Percentages of Stars in Common among the Different Selection Samples

| | Thin | | | | | Thick | | | | |
|---|---|---|---|---|---|---|---|---|---|---|
| Selection | $N_{star}$ | C % | K % | O % | All % | $N_{star}$ | C % | K % | O % | All % |
| C | 1267 | | 72 | 50 | 48 | 99 | | 32 | 14 | 12 |
| K | 1356 | 67 | | 65 | 45 | 196 | 16 | | 36 | 6 |
| O | 934 | 68 | 95 | | 66 | 90 | 15 | 80 | | 13 |

**Note.** C–chemical selection; K–kinematical selection; O–orbital selection.

disk stars for the selection based on orbital parameters is an effect of the selection itself and, therefore, can be artificial.

These results are in agreement with Bensby et al. (2014), who did not find any low-$\alpha$ star at $R_{med} < 7$ kpc, and with Kordopatis et al. (2015), who found very few low-$\alpha$ stars for $R < 7.5$ kpc. Assuming that $R_{med}$ is a measure of the distance from the Galactic center of the stellar birthplace, its increase with decreasing age for thick-disk stars can be explained, as evidence for "inside-out" (Nuza et al. 2019) formation scenarios as found also by Bergemann et al. (2014). This fact, together with the $|Z_{max}|$ versus age behaviors that suggest an "upside-down" (Freudenburg et al. 2017) formation scenario of the disk components of our Galaxy, indicates that, radially, the central disk was formed before the outer disk and, vertically, the thick disk was formed before the thin disk.

## 7. Conclusions

In this paper we investigated the carbon abundance in the thin and thick disks of our Galaxy. The analysis is based on a sample of 2133 dwarf stars from the *Gaia*–ESO Survey. Their carbon abundances were derived by comparing the observed UVES spectra with "on-the-fly" computed synthetic spectra obtained from fully consistent atmosphere models. The designation of stars to the thin- or thick-disk populations was addressed by adopting three different selection approaches, i.e., a chemical one based on positions in the [Mg/Fe]–[Fe/H] plane, a kinematical one based on stellar Galactic velocities, and a third one based on orbital parameters.

The three different selections led to different samples of candidate thin- and thick-disk stars:

1. Chemical selection identified 1267 thin-disk stars ($Thin^C$ sample) and 99 thick-disk stars ($Thick^C$ sample).
2. Kinematical selection identified 1356 thin-disk stars ($Thin^K$ sample) and 196 thick-disk stars ($Thick^K$ sample).
3. Selection based on orbital parameters identified 934 thin-disk stars ($Thin^O$ sample) and 90 thick-disk stars ($Thick^O$ sample).

Only 620 and 12 stars are classified as thin- or thick-disk stars, respectively, by using all three selections. The low number of thick-disk stars with unanimous classification is, in particular, due to the poor agreement between the chemical selection, i.e., high [Mg/Fe], and each of the other two (see Table 3). Even if the different selections produced not fully concordant lists of candidates, the chemical and kinematical general trends of the thin and $thick^{C,K,O}$ samples display quite common behaviors, and our results show the following:

1. In all cases, our thin- and thick-disk stars show different carbon abundances and [C/H], [C/Fe], and [C/Mg] abundances ratios.
2. Our thin- and thick-disk stars span different age intervals, with the latter being, on average, older than the former.
3. The behaviors of [C/H], [C/Fe], and [C/Mg] versus [Fe/H], [Mg/H], and age all suggest that C is primarily produced in massive stars like Mg, but the rise of [C/Mg] for young thin-disk stars indicates that low-mass stars may also play a role in providing carbon in the Galactic thin disk.
4. The analysis of the orbital parameters $R_{med}$ and $|Z_{max}|$ supports an "inside-out" and "upside-down" formation scenario for the disks of Milky Way.

The data used in this paper, together with the derived atmospheric parameter values, are parts of the full data set from the GES survey and will be published through the ESO archive as required for any ESO public surveys. All the GES spectra will be publicly available early in 2020, the astrophysical parameters and abundances shortly thereafter.

This work is based on data products from observations made with ESO Telescopes at the La Silla Paranal Observatory under program ID 188.B-3002. These data products have been processed by the Cambridge Astronomy Survey Unit (CASU) at the Institute of Astronomy, University of Cambridge, and by the FLAMES/UVES reduction team at INAF/Osservatorio Astrofisico di Arcetri. These data have been obtained from the *Gaia*–ESO Survey Data Archive, prepared and hosted by the Wide Field Astronomy Unit, Institute for Astronomy, University of Edinburgh, which is funded by the UK Science and Technology Facilities Council. This work was partly supported by the European Union FP7 program through ERC grant No. 320360 and by the Leverhulme Trust through grant RPG-2012-541. We acknowledge the support from INAF and Ministero dell' Istruzione, dell' Università e della Ricerca (MIUR), in the form of the grant "Premiale VLT 2012." The results presented here benefit from discussions held during the *Gaia*–ESO workshops and conferences supported by the ESF (European Science Foundation) through the GREAT Research Network Program.

This work has made use of data from the European Space Agency (ESA) mission *Gaia* (https://www.cosmos.esa.int/gaia), processed by the *Gaia* Data Processing and Analysis Consortium (DPAC, https://www.cosmos.esa.int/web/gaia/dpac/consortium). Funding for the DPAC has been provided by national institutions, in particular the institutions participating in the *Gaia* Multilateral Agreement.

This work received partial financial support from PRIN MIUR 2010–2011 project "The Chemical and Dynamical Evolution of the Milky Way and Local Group Galaxies," prot. 2010LY5N2T, and by the National Institute for Astrophysics (INAF) through the grant PRIN-2014 ("The *Gaia*–ESO Survey"). M.C. acknowledges financial support from CONACyT grant CB-2015-256961. T.B. was supported by the project grant "The New Milky Way" from the Knut and Alice Wallenberg Foundation. U.H. acknowledges support from the Swedish National Space Agency (SNSA/Rymdstyrelsen). S.G.S acknowledges the support by Fundação para a Ciência e Tecnologia (FCT) through national funds and a research grant (project ref. UID/FIS/04434/2013, and PTDC/FIS-AST/

7073/2014). S.G.S. also acknowledges the support from FCT through Investigador FCT contract of reference IF/00028/2014 and POPH/FSE (EC) by FEDER funding through the program "Programa Operacional de Factores de Competitividade—COMPET."

This research uses the facilities of the Italian Center for Astronomical Archive (IA2) operated by INAF.

*Facilities:* VLT:Kueyen, UVES.

*Software:* SPECTRUM (v2.76f; Gray & Corbally 1994), ATLAS12 (Kurucz 2005).

## ORCID iDs

Mariagrazia Franchini https://orcid.org/0000-0001-5611-2333
Carlo Morossi https://orcid.org/0000-0002-3319-6375
Paolo Di Marcantonio https://orcid.org/0000-0003-3168-2289
Amelia Bayo https://orcid.org/0000-0001-7868-7031
Angela Bragaglia https://orcid.org/0000-0002-0338-7883
Francesco Calura https://orcid.org/0000-0002-6175-0871
Georges Kordopatis https://orcid.org/0000-0002-9035-3920
Donatella Romano https://orcid.org/0000-0002-0845-6171
Giovanni Carraro https://orcid.org/0000-0002-0155-9434

## References

Adibekyan, V. Z., Figueira, P., Santos, N. C., et al. 2013, A&A, 554, A44
Adibekyan, V. Z., Santos, N. C., Sousa, S. G., & Israelian, G. 2011, A&A, 535, L11
Akerman, C. J., Carigi, L., Nissen, P. E., Pettini, M., & Asplund, M. 2004, A&A, 414, 931
Amarsi, A. M., Barklem, P. S., Collet, R., Grevesse, N., & Asplund, M. 2019a, A&A, 624, A111
Amarsi, A. M., Nissen, P. E., Asplund, M., Lind, K., & Barklem, P. S. 2019b, A&A, 622, L4
Amarsi, A. M., Nissen, P. E., & Skúladóttir, Á 2019c, A&A, 630, A104
Angus, R., Morton, T. D., Foreman-Mackey, D., et al. 2019, AJ, 158, 173
Asplund, M. 2005, ARA&A, 43, 481
Bensby, T., & Feltzing, S. 2006, MNRAS, 367, 1181
Bensby, T., Feltzing, S., Gould, A., et al. 2017, A&A, 605, A89
Bensby, T., Feltzing, S., & Lundström, I. 2003, A&A, 410, 527
Bensby, T., Feltzing, S., & Oey, M. S. 2014, A&A, 562, A71
Bergemann, M., Ruchti, G. R., Serenelli, A., et al. 2014, A&A, 565, A89
Binney, J. 2010, MNRAS, 401, 2318
Buder, S., Lind, K., Ness, M. K., et al. 2019, A&A, 624, A19
Calura, F., & Menci, N. 2009, MNRAS, 400, 1347
Carigi, L., Peimbert, M., Esteban, C., & García-Rojas, J. 2005, ApJ, 623, 213
Casagrande, L., Schönrich, R., Asplund, M., et al. 2011, A&A, 530, A138
Cescutti, G., Matteucci, F., François, P., & Chiappini, C. 2007, A&A, 462, 943
Cescutti, G., Matteucci, F., McWilliam, A., & Chiappini, C. 2009, A&A, 505, 605
Chiappini, C., Matteucci, F., & Meynet, G. 2003a, A&A, 410, 257
Chiappini, C., Romano, D., & Matteucci, F. 2003b, MNRAS, 339, 63
De Silva, G. M., Freeman, K. C., Bland-Hawthorn, J., et al. 2015, MNRAS, 449, 2604
Dekker, H., D'Odorico, S., Kaufer, A., Delabre, B., & Kotzlowski, H. 2000, Proc. SPIE, 4008, 534
Delgado Mena, E., Israelian, G., González Hernández, J. I., et al. 2010, ApJ, 725, 2349
Drimmel, R., Cabrera-Lavers, A., & López-Corredoira, M. 2003, A&A, 409, 205
Evans, D. W., Riello, M., De Angeli, F., et al. 2018, A&A, 616, A4
Ferguson, D., Gardner, S., & Yanny, B. 2017, ApJ, 843, 141
Franchini, M., Morossi, C., Di Marcantonio, P., et al. 2018, ApJ, 862, 146
Freudenburg, J. K. C., Weinberg, D. H., Hayden, M. R., & Holtzman, J. A. 2017, ApJ, 849, 17
Fuhrmann, K. 1998, A&A, 338, 161
Fulbright, J. P. 2002, AJ, 123, 404
Fux, R. 2001, A&A, 373, 511
Gaia Collaboration, Brown, A. G. A., Vallenari, A., et al. 2018, A&A, 616, A1
Gavilán, M., Buell, J. F., & Mollá, M. 2005, A&A, 432, 861
Gilmore, G., Randich, S., Asplund, M., et al. 2012, Msngr, 147, 25
Gonneau, A., Lançon, A., Trager, S. C., et al. 2016, A&A, 589, A36
Gray, R. O., & Corbally, C. J. 1994, AJ, 107, 742
Grevesse, N., Asplund, M., & Sauval, A. J. 2007, SSRv, 130, 105
Grisoni, V., Spitoni, E., Matteucci, F., et al. 2017, MNRAS, 472, 3637
Gustafsson, B., Karlsson, T., Olsson, E., Edvardsson, B., & Ryde, N. 1999, A&A, 342, 426
Haywood, M., Di Matteo, P., Lehnert, M. D., Katz, D., & Gómez, A. 2013, A&A, 560, A109
Henry, R. B. C., Edmunds, M. G., & Köppen, J. 2000, ApJ, 541, 660
Howes, L. M., Lindegren, L., Feltzing, S., Church, R. P., & Bensby, T. 2019, A&A, 622, A27
Iben, I. J. 1965, ApJ, 142, 1447
Johnston, K. V. 1998, ApJ, 495, 297
Johnston, K. V., Hernquist, L., & Bolte, M. 1996, ApJ, 465, 278
Jørgensen, B. R., & Lindegren, L. 2005, A&A, 436, 127
Kordopatis, G., Wyse, R. F. G., Gilmore, G., et al. 2015, A&A, 582, A122
Kurucz, R., & Bell, B. 1995, Atomic Line Data (Cambridge, MA: Smithsonian Astrophysical Observatory), 23
Kurucz, R. L. 2005, MSAIS, 8, 14
Kurucz, R. L., & Peytremann, E. 1975, SAOSR, 362, 1, (KP)
Liang, Y. C., Zhao, G., & Shi, J. R. 2001, A&A, 374, 936
Magrini, L., Randich, S., Kordopatis, G., et al. 2017, A&A, 603, A2
Magrini, L., Vincenzo, F., Randich, S., et al. 2018, A&A, 618, A102
Majewski, S. R., Schiavon, R. P., Frinchaboy, P. M., et al. 2017, AJ, 154, 94
Matteucci, F., & Chiappini, C. 2003, in ASP Conf. Ser. 304, CNO in the Universe, ed. C. Charbonnel, D. Schaerer, & G. Meynet (San Francisco, CA: ASP), 384
Mattsson, L. 2010, A&A, 515, A68
McMillan, P. J. 2017a, MNRAS, 465, 76
McMillan, P. J. 2017b, MNRAS, 466, 174
Meléndez, J., Asplund, M., Gustafsson, B., & Yong, D. 2009, ApJL, 704, L66
Meynet, G., & Maeder, A. 2002, A&A, 390, 561
Miller, M. H., Wilkerson, T. D., Roig, R. A., & Bengtson, R. D. 1974, PhRvA, 9, 2312, (MWRB)
Nissen, P. E. 2004, Origin and Evolution of the Elements, ed. A. McWilliam & M. Rauch, 154
Nissen, P. E., Chen, Y. Q., Carigi, L., Schuster, W. J., & Zhao, G. 2014, A&A, 568, A25
Nissen, P. E., & Gustafsson, B. 2018, A&ARv, 26, 6
Nuza, S. E., Scannapieco, C., Chiappini, C., et al. 2019, MNRAS, 482, 3089
Pasquini, L., Avila, G., Blecha, A., et al. 2002, Msngr, 110, 1
Pont, F., & Eyer, L. 2004, MNRAS, 351, 487
Randich, S., Gilmore, G. & Gaia–ESO Consortium 2013, Msngr, 154, 47
Randich, S., Tognelli, E., Jackson, R., et al. 2018, A&A, 612, A99
Reddy, B. E., Lambert, D. L., & Allende Prieto, C. 2006, MNRAS, 367, 1329
Romano, D., Karakas, A. I., Tosi, M., & Matteucci, F. 2010, A&A, 522, A32
Romano, D., Matteucci, F., Zhang, Z.-Y., Ivison, R. J., & Ventura, P. 2019, MNRAS, 490, 2838
Sacco, G. G., Morbidelli, L., Franciosini, E., et al. 2014, A&A, 565, A113
Salaris, M., Pietrinferni, A., Piersimoni, A. M., & Cassisi, S. 2015, A&A, 583, A87
Schönrich, R., Binney, J., & Dehnen, W. 2010, MNRAS, 403, 1829
Shi, J. R., Zhao, G., & Chen, Y. Q. 2002, A&A, 381, 982
Smiljanic, R., Korn, A. J., Bergemann, M., et al. 2014, A&A, 570, A122
Soderblom, D. R. 2010, ARA&A, 48, 581
Soubiran, C., Bienaymé, O., & Siebert, A. 2003, A&A, 398, 141
Spitoni, E., Silva Aguirre, V., Matteucci, F., Calura, F., & Grisoni, V. 2019, A&A, 623, A60
Suárez-Andrés, L., Israelian, G., González Hernández, J. I., et al. 2017, A&A, 599, A96
Swan, W. 1857, Transactions of the Royal Society of Edinburgh, 21, 411
van den Hoek, L. B., & Groenewegen, M. A. T. 1997, A&AS, 123, 305
Widrow, L. M., Gardner, S., Yanny, B., Dodelson, S., & Chen, H.-Y. 2012, ApJ, 750, L41
Wilson, M. L., Helmi, A., Morrison, H. L., et al. 2011, MNRAS, 413, 2235